CHEMISTRY OF MATERIALS

Article

pubs.acs.org/cm

Shape Memory Superelastic Poly(isocyanurate-urethane) Aerogels (PIR-PUR) for Deployable Panels and Biomimetic Applications

Suraj Donthula, Chandana Mandal, Theodora Leventis,[†] James Schisler,[†] Adnan Malik Saeed, Chariklia Sotiriou-Leventis,* and Nicholas Leventis*

Department of Chemistry, Missouri University of Science and Technology, Rolla, Missouri 65409, United States

Supporting Information

ABSTRACT: Shape memory polymers (SMPs) remember and return to an original shape when triggered by a suitable stimulus, typically a change in temperature. They are pursued as cost-effective, low-density, higher-strain-tolerant alternatives to shape memory alloys. Arguably, *porous* SMPs may offer the near-ultimate refinement in terms of density reduction. To that end, shape memory polymeric aerogels (SMPAs) may offer a viable approach. The necessary condition for SMPs is rubber-like superelasticity, which is introduced via cross-linking. Cross-linking is also a necessary condition for inducing phase separation during solution-phase polymerization of suitable monomers into 3D nanoparticle networks. Such networks form the skeletal frameworks of polymeric aerogels. Those principles were explored here with rigid trifunctional isocyanurate cross-linking nodes between flexible urethane tethers from four short oligomeric derivatives of ethylene glycol: $H(OCH_2CH_2)_nOH$ ($1 \leq n \leq 4$). Formation of self-supporting 3D particle networks depended on the solubility of the developing polymer, which translated into specific combinations of the diol, monomer concentration, and composition of the solvent (CH_3CN/acetone mixtures). Those parameters were varied systematically using statistical design-of-experiments methods. The skeletal frameworks of the resulting poly(isocyanurate-urethane) (PIR-PUR) aerogels consisted of micrometer-size particles. Bulk densities were in the 0.2−0.4 g cm^{-3} range, and typical porosities were between 70% and 80% v/v. Glass transition temperatures (T_g) varied from about 30 (n = 4) to 70 °C (n = 1). At and above T_g, all SMPAs showed rubber-like elasticity. They also became stiffer after the first stretching cycle, which was traced to maximization of H-bonding interactions (NH···O═C and NH···$O(CH_2)_2$). Below the T_g zone, the elastic modulus of all formulations decreased by about 1000 fold. That property gave rise to a robust shape memory effect (SME), the quality of which was evaluated via several figures of merit that were calculated from tensile stretching data over five temperature cycles between T_g + 10 °C and T_g − 40 °C. All thermomechanical testing was carried out with dynamic mechanical analysis (DMA). The strain fixity was always >98%, pointing to very low creep. After the first cycle, strain recovery (a measure of fatigue) improved from 80−90% to about 100%, and the fill factor, a cumulative index of performance, reached 0.7, which is in the range of fast elastomers. The robust shape memory effect was demonstrated with deployable panels and bionic hands capable of mimicking coordinated muscle function.

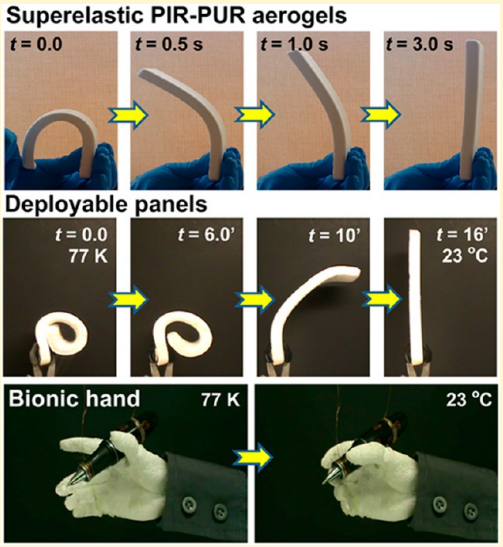

1. INTRODUCTION

Shape memory materials (SMM) remember and return to an original shape. The transition is triggered by light,[1,2] electric[3,4] or magnetic fields,[5] but most frequently though by a change in temperature.[6] The two main classes of SMMs are shape memory alloys (SMAs) and shape memory polymers (SMPs). Application areas range from aerospace (deployable structures),[7] to biomedicine (implantable devices,[8,9] surgical sutures,[10] drug delivery vehicles),[11] to transportation,[12] construction,[13] electronic,[14] textile[15] and various consumer product industries (e.g., as lightweight actuators).[16,17]

The first SMM was a Au−Cd alloy (1930s).[18] Nitinol (a Ni−Ti alloy), arguably the most well-studied material in that class, was introduced in the 1960s.[19,20] Nitinol is a superelastic material, meaning that it recovers its shape after extreme deformations, e.g., after bending by 180°.[21] Superelasticity is a necessary condition for the shape memory effect but not sufficient: just so it happens, the martensitic phase of Nitinol, which is brought about by lattice deformation under shear stress, is also stable at lower temperatures. Thus, deformation at a higher temperature followed by cooling "freezes" Nitinol to a temporary shape that is retained even after stress is removed. By raising the temperature, the martensitic phase returns to the normal stress-free austenitic phase of the material and the object recovers its original shape. SMAs develop high recovery

Received: March 13, 2017
Published: May 2, 2017

DOI: 10.1021/acs.chemmater.7b01020
Chem. Mater. 2017, 29, 4461−4477

stresses, in the range of 50−500 MPa, on the downside though they are heavy and costly and their recoverable transformation strains are low (usually <10%—above that level, deformation causes unrecoverable lattice slippage).[22]

SMPs are high strain-tolerant, lightweight alternatives to SMAs. The first SMP was disclosed in a 1941 patent and was based on a methacrylic acid ester for dental applications.[23] The familiar cross-linked polyethylene-based heat-shrinking tubing was introduced in the 1960s;[24−26] however, systematic research on SMPs started gaining momentum only in the 1990s.[27−29] Superelasticity is again a necessary condition for the shape memory effect, but here it is more commonly referred to as "rubber-like elasticity".[30] Rubber-like elasticity implies that superelastic polymers are elastomers; thus, their response to tensile stress is associated with rigid covalent cross-linking nodes between extendable (i.e., linear) polymeric strands. However, for such elastic behavior, polymeric strands must be free to move in the first place; therefore, the polymer must be amorphous and above its glass transition temperature. Thereby, in the simplest form, if an elastomer with a glass transition temperature (T_g) within a range of interest—typically at room temperature or slightly above—is first deformed and then cooled below T_g, segmental motion of the polymeric chains stops and covalent cross-linking nodes cannot pull the polymer back to its original shape. Raising the temperature back above T_g allows the covalent cross-linking nodes to do their job.

Those principles have been implemented with a wide range of polymers and combinations thereof in blends and in layers, utilizing for the shape memory effect glass transitions but also crystallization phenomena.[31−33] SMPs include polyacrylate copolymers,[34] segmented polyurethanes,[35,36] and polyurethane ionomers,[37] poly(ether ether ketone) ionomers,[38] epoxy-based polymers,[39] thio−ene-based polymers,[40] cross-linked polycyclooctene,[41] polynorbornene,[42] cross-linked ethylene-vinyl acetate copolymers,[43] and various styrene-based polymers.[44]

Perhaps, the ultimate refinement in terms of weight reduction in SMM may involve porous polymers. A special class of materials in that category is classified as aerogels and is prepared by drying wet-gels under conditions that preserve the volume of the gel into the final dry object. That process typically involves converting the pore-filling liquid into a supercritical fluid (SCF) that is vented of as a gas. In turn, wet-gels are prepared via a sol−gel process that involves solution polymerization of suitable multifunctional monomers in a suitable solvent.[45,46] For this, covalent cross-linking, *in principle similar to what makes polymers elastomeric*, renders the growing polymer insoluble in the polymerization medium and induces phase separation of colloidal polymeric nanoparticles that bear active functional groups on their surface. Moving around randomly, eventually, those polymeric nanoparticles find one another and get linked via reaction of their surface functional groups into a 3D network that comprises the skeletal framework of the aerogel. By this discussion so far it may be perceived that shape memory aerogels are mere SMPs in aerogel form. In reality, however, there are conflicting requirements between those two classes of materials. For shape memory elastomers the polymeric strands between cross-linking nodes are typically long by aerogel standards, and if that chemistry is transplanted directly into aerogel synthesis, one will face the fact that longer tethers increase the solubility of the developing polymer. In turn, that causes accumulation of a secondary polymeric layer on the surface of the primary network via reaction of soluble oligomers in the pores with the active functional groups on the nanoparticles.[47−49] Upon deswelling during drying, that continuous secondary layer of polymer pulls the particle network together, causing collapse into a more or less dense plastic. Clearly, there is a need for a fine balance between the factors that render a polymer superelastic and at the same time sufficiently insoluble and able to form a sturdy aerogel skeletal framework. The unsatisfied quest for that balance is what has rendered shape memory aerogels elusive. A closer look at superelasticity and aerogels is therefore in order.

Superelastic aerogels have been described mostly with silica or silica−organic hybrids.[50−53] The phenomenon has been associated invariably with a spring-back effect after compression—*not* tension. We are aware of only one recent example of thiol−ene-based aerogels that went through temperature cycles and showed size fixing upon cooling and recovery upon heating.[54] Again, those materials were tested only under compression. However, folding/unfolding and other complicated deformations typically associated with the shape memory effect require rubber-like superelasticity under tension. In that context, there are numerous literature reports about flexible polymeric aerogels, most notably polyimides,[55] and certain isocyanate-derived aerogels based on polyureas[56] and polyurethanes[49,57] that could be bent by 180°, but rubber-like elasticity is still lacking: only a small fraction, if any, of that deformation could be recovered after stress was removed. Nevertheless, there is a particular class of isocyanate-derived polymers, polyisocyanurates (PIRs), which warrants special attention. PIRs come from trimerization of isocyanates and, because of their high thermal stability and low flammability, are pursued as insulation foams, coatings, and adhesives.[58−61] On the down side though, PIRs are friable—they can be easily crumbled. To overcome that issue, commercial PIRs are urethane-modified polymers made by mixing an excess of a diisocyanate with a diol and a suitable catalyst. Reaction of the diisocyanate both with itself and with the diol yields isocyanurate rings linked by urethane tethers. In those poly(isocyanurate-urethane) polymers (PIR-PUR), isocyanurate rings play the role of covalent nodes. PIR-PURs are no longer friable and in many cases elastomeric.[62,63]

Along the molecular design principles of PIR-PUR, Scheme 1 shows the monomers and the reaction pathway employed in this study toward shape memory aerogels. For closer control of the properties of the polymer, we opted against simultaneous formation of the isocyanurate rings and the polyurethane tethers. Instead, the isocyanurate cross-linking nodes were introduced separately as part of the monomer by using a commercial triisocyanate derivative of aliphatic hexamethylene diisocyanate (N3300A—see Scheme 1), which combines the rigidity of the isocyanurate ring with the flexibility of the $-(CH_2)_6-$ tethers. The diols were variable-length derivatives of ethylene glycol (EG) and chosen over, for example, hydrocarbon alternatives because of the possibility for H-bonding with the urethane groups of neighboring polymeric branches. Chances for H-bonding, which could be enhanced with longer EG-derived diols, would reduce molecular slippage and macroscopic creep, thus favoring elastic over plastic behavior. On the other hand, though, longer diols would enhance segmental motion of internodal tethers, which could be desirable in terms of lowering glass transition temperatures into a useful range, but they could also increase plasticity. Furthermore, it was also understood that increasing the length of the diol would necessarily increase the solubility of the

DOI: 10.1021/acs.chemmater.7b01020
Chem. Mater. 2017, 29, 4461−4477

Scheme 1. (A) Reagents (triisocyanate, ethylene glycol-based diols); (B) Reaction Pathway to Isocyanurate Cross-Linking Nodes Linked with Urethane Tethers (PIR-PUR)

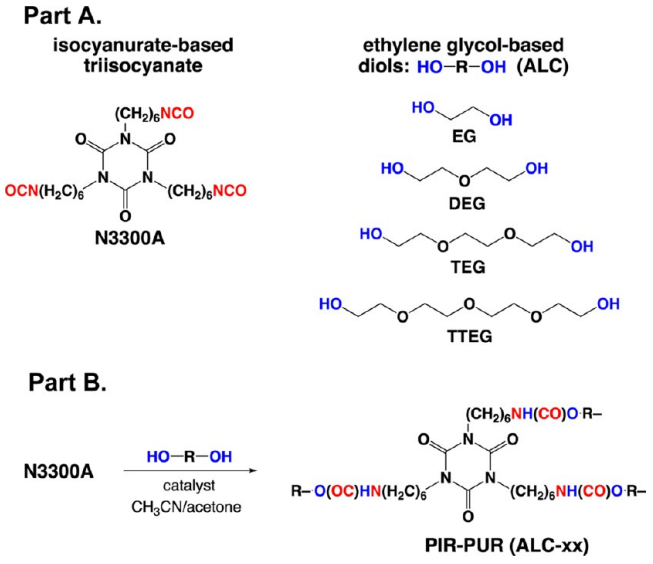

developing polymer, which would increase the particle size and consequently decrease surface areas and would compromise thermal conductivity. However, such a departure from typical aerogel properties was deemed acceptable given our objective toward low-density shape memory materials rather than more conventional aerogel applications (e.g., in thermal insulation). In practice, particle sizes and secondary polymer accumulation on the primary network were controlled not only via the chemical identity of the diol but also via the sol concentration and via the gelation solvent, which was varied from pure acetonitrile to a 1:1 v/v mixture of acetonitrile/acetone.

Materials are described in terms of their chemical composition, micromorphology, and thermomechanical properties. The shape memory effect was quantified with several figures of merit that include the shape fixity ratio, the strain recovery ratio, the strain recovery rate, and the fill factor. Varying the alcohol affected the glass transition temperature, which in the case of TEG translated into shape-recovery activated at room temperature. That accounts for the most dramatic demonstration of the shape memory effect in terms of potential applications in deployable panels and biomimetic devices.

2. RESULTS AND DISCUSSION

2.1. Synthesis and Chemical Identification of Polyisocyanurate Aerogels. The reaction of Scheme 1B was implemented according to the protocol of Scheme 2A. Urethane formation was catalyzed by dibutyltin dilaurate (DBTDL) in a 1:120 mol/mol ratio relative to N3300A, and gelation took place at room temperature. Monomers were used at their stoichiometric amounts (triisocyanate:diol = 2:3 mol/mol). Wet-gels were aged up to 16 h to ensure complete reaction and dried to aerogels by extracting the pore-filling solvent with liquid CO_2, which, at the end, was converted to a supercritical fluid (SCF) and vented off as a gas. Sols were prepared in acetonitrile:acetone mixtures from 50:50 v/v to pure CH_3CN. The total monomer concentration was varied between 15% and 25% w/w. The ranges of the solvent ratio and the monomer concentration were based on screening experiments with TEG-based PIR-PUR aerogels, in which we looked for low-density materials demonstrating room-temperature rubber-like superelasticity similar to that of alloys,[21] as shown in Figure 1. Such TEG-based samples either above the selected concentration range or prepared in sols consisting of more than 50% v/v acetone seemed to collapse into dense "plastics." Below the selected concentration range, if sols could still form gels, the resulting aerogels did not seem to have the strength to "lift" themselves up as in Figure 1. Samples prepared in pure acetonitrile did not seem to show optimal performance in terms of their recovery time (Figure 1). Since those two exploratory variables, monomer concentration and solvent composition, seemed to have a similar effect in terms of their ability to form low-density rubber-like superelastic materials, it was deemed reasonable that their effects were coupled. Thereby, for the purposes of the protocol of Scheme 2A, sample preparation with each diol was guided by response surface methodology implemented with a central composite

Scheme 2. (A) Synthetic Protocol of PIR-PUR Aerogels (ALC-xx); (B) ALC-xx Formulation According to a Central Composite Rotatable Design Model (CCRD)[a]

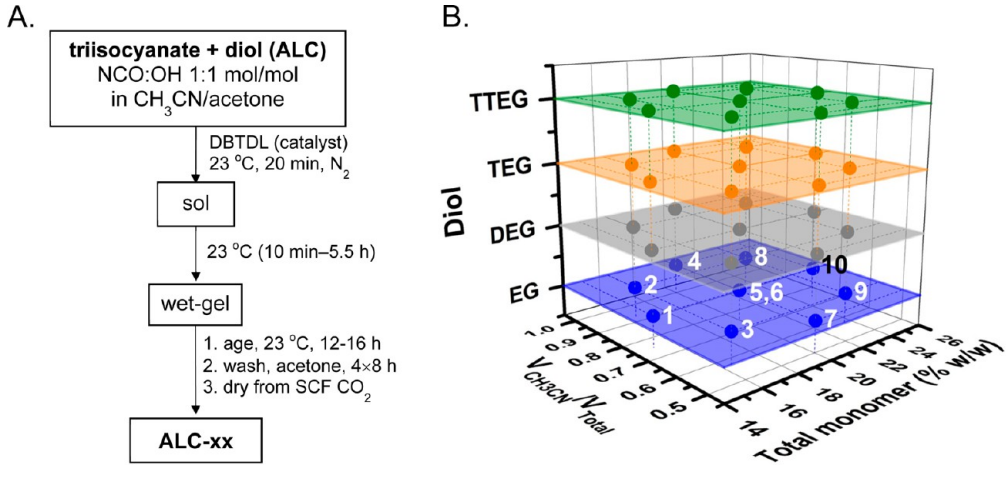

[a]Independent (exploratory) variables: volume fraction of CH_3CN in the sol ($0.5 \leq V_{CH3CN}/V_{Sol} \leq 1.0$), and total monomer concentration in the sol (15% w/w ≤ total monomer ≤ 25% w/w).

DOI: 10.1021/acs.chemmater.7b01020
Chem. Mater. 2017, 29, 4461−4477

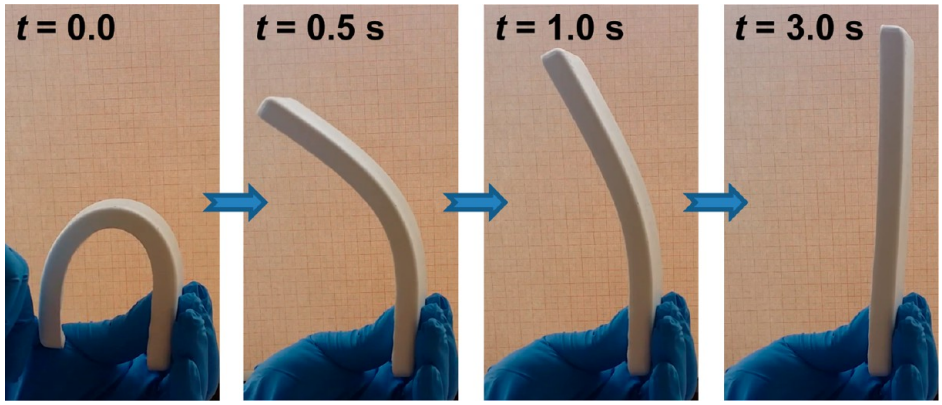

Figure 1. Demonstration of room-temperature superelasticity with a **TEG-8** sample (2" × 8" × 0.4", ρ_b = 0.41 ± 0.02 g cm^{-3}, Π = 67 ± 1% v/v). Photographs are selected frames from Movie S.1 shown in the Supporting Information.

rotatable design model (CCRD—see Appendix I in the Supporting Information),[64−66] in which point selection in the domain of the exploratory variables was carried out using the JMP11 software package,[67] from the perspective of a subsequent quadratic dependence of the derived properties (e.g., density, porosity, modulus, etc.) on the exploratory variables.[68] Individual samples are referred to as **ALC-xx**, according to their diol (ALC) and their position (**-xx**) on the rotatable domain. The design space is summarized in Scheme 2B. The exact formulations are tabulated in Tables S.1 and S.2 of Appendix I in the Supporting Information, along with the phenomenological gelation times. Here, in brief, **ALC-1**/**ALC-10** correspond to the middle V_{CH3CN}/V_{sol_Total} ratio (0.75) and the low/high monomer concentrations, respectively. The central point of the design was repeated twice (**ALC-5** and **ALC-6**). Even-numbered **ALC-2**, **ALC-4**, and **ALC-8** correspond to higher V_{CH3CN} sols. Odd-numbered **ALC-3**, **ALC-7**, and **ALC-9** correspond to acetone-rich sols.

The chemical composition of **ALC-xx** was confirmed with solid-state CPMAS ^{13}C and ^{15}N NMR (Figure 2). Insight to noncovalent interactions (H-bonding) was obtained with ATR-FTIR and is discussed in section 2.3.2 below in conjunction with the thermomechanical properties of **ALC-xx**. The N^{13}CO and ^{15}NCO resonances of the isocyanate (expected at 122 and 28.5 ppm, respectively) were absent from all ^{13}C and ^{15}N NMR spectra, pointing to complete reaction. The ^{13}C NMR resonances at 149.8 and 157.2 ppm were assigned to the isocyanurate and the urethane carbonyl (−NH(C═O)O−), respectively. The resonances at 61.8 and 70.6 ppm were assigned to the aliphatic carbons of ALC, and the relative intensity of the two resonances changed from **EG-xx** to **TTEG-xx**, as expected from the number of internal vs terminal −OCH$_2$CH$_2$− groups sandwiched between two urethane groups. The remaining two peaks in the aliphatic region, at 43.0 and 27.7 ppm, were assigned to the −CH$_2$− groups of N3300A (Scheme 1A). Interestingly, the urethane carbonyl resonance at 157.2 ppm (−NH(C═O)O−) was sharper in **EG-xx** and **DEG-xx** and became progressively broader in **TEG-xx** and **TTEG-xx**. In the solid-state ^{15}N NMR spectra, the resonance at 138.0 ppm was assigned to the isocyanurate ring and the one at 80.5 ppm to the urethane nitrogen. No resonance was detected in the 50−60 ppm region that could be assigned to −NH$_2$ from hydrolysis of unreacted −NCO.[56] Just like in the solid-state ^{13}C NMR spectra, again, we noted a progressive peak broadening of the −NH(C═O)O− resonance, which became most prevalent in **TTEG-xx**. Peak broadening in both the ^{13}C and the ^{15}N NMR spectra of the −NH(C═O)O− group signifies that as the length of ALC increased, urethane groups found themselves in more diverse environments and/or H-bonded.

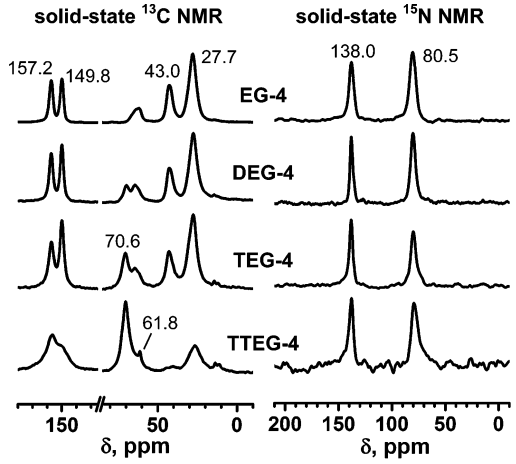

Figure 2. Solid-state CPMAS ^{13}C and ^{15}N NMR of samples as indicated.

2.2. General Material Properties, Micromorphology, and Growth Mechanism of ALC-xx from an Exploratory Variable Perspective. Relevant material properties of **ALC-xx** are summarized in Table S.3 of Appendix II in the Supporting Information. Here, in graph form, Figure 3 compares shrinkage, bulk densities, and porosities of all **ALC-xx** as a function of their position in the domain of the exploratory variables (i.e., the sol composition). For quick reference, that domain is reproduced as a separate frame in Figure 3. Most **ALC-xx** aerogels shrunk roughly 20−25% in linear dimensions relative to the molds. Samples that stand out are all **TTEG-xx** aerogels, except **TTEG-2** and **TTEG-4** (pointed at by gray arrows), and **TEG-7**, **TEG-9**, and **TEG-10** (pointed at by blue arrows). **TTEG-2** and **TTEG-4** shrunk less (29% and 31%, respectively) than the other **TTEG-xx** (40−50%); **TEG-7**, **TEG-9**, and **TEG-10** shrunk more than the other **TEG-xx** samples, in fact in the **TTEG-xx** range (40−50%). Importantly, *all* shrinkage in *all* samples was observed *exclusively* during drying: even the collapsed samples of Figure 3 (i.e., those that shrunk excessively) showed no shrinkage during solvent exchange, suggesting that (a) all four polymers were swollen in their wet-

DOI: 10.1021/acs.chemmater.7b01020
Chem. Mater. 2017, 29, 4461−4477

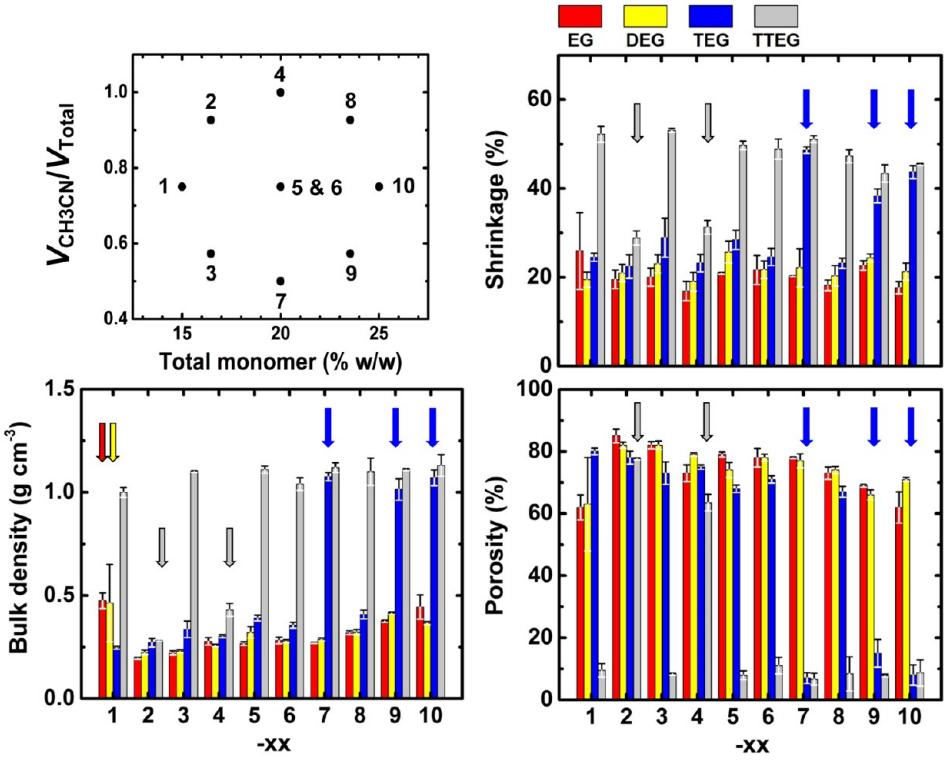

Figure 3. Shrinkage, bulk density, and porosity data for all **ALC-xx** samples in the domain of the two exploratory variables (total monomer concentration and solvent ratio). Data were taken from Table S.3 of the Supporting Information. Color-coded arrows point at samples that break the respective "trends" and are discussed in the text.

gel state and (b) no major reorganization of the nanostructure took place during solvent exchanges.[69] High shrinkages were accompanied by high bulk densities (ρ_b)—in some cases >1.0 g cm^{-3}—and low porosities (Π): in most collapsed samples Π < 10% v/v.[70] At any rate, the vast majority of **EG-xx**, **DEG-xx** and **TEG-xx** were low-density materials (ρ_b < 0.5 g cm^{-3}) with high porosities (mostly 70−80% v/v). Within their respective ranges, ρ_b and Π followed the general upward and downward trends expected by increasing the sol concentration. Two notable exceptions were **EG-1** and **DEG-1** (pointed with color-coded arrows, red and yellow): although their densities/porosities were not excessive (high/low, respectively), those two samples did stand out with densities disproportionally higher and porosities disproportionally lower than those of the rest of the **EG-xx** and **DEG-xx**. Those two samples were at the lower end of the isocyanate concentration range, and upon closer examination they appeared chalky and could not be machined for mechanical testing, and by looking back at the gelation process it was noticed that the reaction products looked more like loose precipitates (flocs) rather than colloidal gels.

Overall, considering all information above together, longer TTEG generally caused excessive shrinkage, which, in two cases, **TTEG-2** and **TTEG-4**, could be controlled via the two exploratory variables, namely, by keeping the TTEG concentration low in combination with CH_3CN-rich sols. Similarly, the three **TEG-xx** samples that shrunk excessively (**TEG-7**, **TEG-9**, and **TEG-10**) were among those from high TEG concentration sols, in combination with acetone-rich solvent. Clearly, as it has been alluded to already from the preliminary runs (section 2.1), the effects of the monomer concentration and the solvent composition were coupled.

Excluding only **EG-1** and **DEG-1** (i.e., the two samples that seemingly came from flocs), quadratic fitting of ρ_b to monomer concentration (X_1) and solvent ratio (X_2) according to eq 1 gave good correlations for all four **ALC-xx**, as shown in Figure 4 ($0.917 \leq R^2 \leq 0.945$).

$$\rho_b = A(X_1)^2 + B(X_2)^2 + C(X_1)(X_2) + D(X_1) + E(X_2) + F \quad (1)$$

Coefficients A−F are cited in Table S.4 of the Supporting Information. It is noteworthy that despite the sudden onset of excessive shrinkage in many samples, density still varied smoothly with X_1 and X_2 in all four **ALC-xx** systems. That finding together with the fact that shrinkage was observed always at the drying stage signify that all **ALC-xx** sols followed similar gelation processes, and the resulting aerogels shared some key microscopic/network characteristics, irrespective of their macroscopic appearance (collapsed or otherwise).

The micromorphology of **ALC-xx** was investigated with SEM (Figure 5). All noncollapsed samples consisted of networks of large micrometer-size spherical particles (see **xx** = 2 column of Figure 5). The contact area around the interparticle neck zones of **EG-xx** was narrow. The particle size first increased in **DEG-xx** relative to **EG-xx** and then decreased (in **TEG-xx** and **TTEG-xx**), while the interparticle neck zones became wider, in essence fusing particles together. The two **TTEG-xx** samples that did not collapse (**TTEG-2** and **TTEG-4**) and the three **TEG-xx** samples that *did* collapse (**TEG-7**, **TEG-9**, and **TEG-10**) became the experimental and conceptual link between the nanostructures of collapsed and noncollapsed samples. Noncollapsed **TTEG-2** consisted of smaller particles than the other **ALC-2** samples, with enhanced merging at the necks. Noncollapsed **TTEG-4** seemed to consist of even smaller particles shrouded by a layer of polymer thicker than the

DOI: 10.1021/acs.chemmater.7b01020
Chem. Mater. 2017, 29, 4461−4477

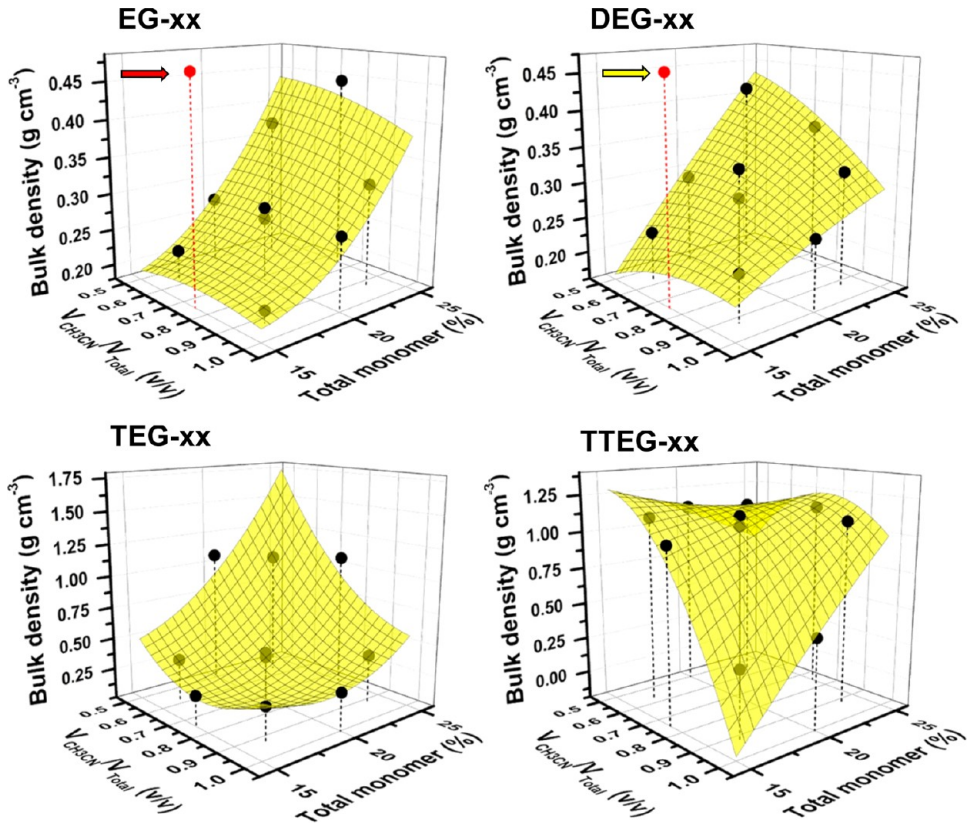

Figure 4. Bulk density data for all **ALC-xx** fitted to the two exploratory variables (monomer concentration and solvent ratio) according to the quadratic model of eq 1. Color-coded arrows point at two samples, **EG-1** and **DEG-2** that could not be fitted by the model. For the coefficients of eq 1 in all four **ALC-xx** refer to Table S.4 in the Supporting Information.

particles themselves. Importantly, the latter was also the common appearance of all **TEG-xx** samples that *did* collapse (see, for example, **TEG-7** in Figure 5 as well as **TEG-9** and **TEG-10** in Figure S.3 of the Supporting Information). To recast and summarize, remnants of particles were still discernible in all collapsed samples, but they were smaller and coated with a thick layer of polymer.

Albeit at different length scales (about 100× smaller than what we are dealing with here), particle fusion at higher sol concentrations, just like what we have been able to visualize in Figure 5, has been inferred previously with numerous other polymeric aerogels by comparing particle sizes calculated based on small-angle X-ray scattering and gas sorption data.[47−49] A universally consistent hypothesis that explains both the previous systems and the morphological evolution noted in Figure 5 involves formation of a primary network of connected spherical particles, followed by accumulation of a secondary polymer layer, preferably at the points of negative curvature—the interparticle necks. That secondary accumulation of polymer takes place via reaction of soluble oligomers or yet unreacted monomer remaining in the pores of the primary network with functional groups on the surface of the particles of the primary network. Clearly, that monomer/oligomer-to-network growth mechanism depends on how fast the primary network is formed, hence on the monomer concentration, and the solubility of the developing polymer. The solubility of the developing polymer depends on the solvent system and the freedom for segmental motion of the polymer chains. In **ALC-xx** the relevant polymeric segments are the $-(CH_2)_6$—NH(CO)—$(OCH_2CH_2)_n$–O(CO)NH–$(CH_2)_6$– tethers ($1 \leq n \leq 4$) connecting the isocyanurate nodes and consist of two fixed-length aliphatic moieties ($-(CH_2)_6-$) and one variable-length ether moiety sandwiched in between. The longer the tether, the more soluble the developing polymer, and secondary polymer accumulation was favored. Similarly, secondary polymer accumulation was enhanced with sols richer in stronger H-bonding acetone, which favors solubilization of the developing polymer.[56,71] Now, it was also observed that the more secondary polymer accumulation, the higher the chances for excessive shrinkage. Given that *all* samples, no exceptions, shrank only during drying, it is reasonable that deswelling of particles was uniform and preserved the morphology and porous structure of the particle network. On the other hand, deswelling of the polymeric layer from secondary accumulation pulled the particle network together causing collapse. Thereby, success in the synthesis of porous PIR-PUR networks is predicated upon the strength of the primary particle network to support itself and resist stresses developing by deswelling of the secondary polymer layer. Overall, a viable aerogel network requires synthetic parameters that reach a balance between particle size and thickness of the polymeric layer from secondary accumulation.

2.3. Thermomechanical Characterization. That was carried out with emphasis on data related to shape memory effects.

2.3.1. Glass Transitions. Glass transitions were determined with temperature scans using dynamic mechanical analysis (DMA) in a tensile test configuration as described in the Experimental Section. Only lower density, noncollapsed samples were considered. That excludes **EG-1**, **DEG-1**, **TEG-**

DOI: 10.1021/acs.chemmater.7b01020
Chem. Mater. 2017, 29, 4461−4477

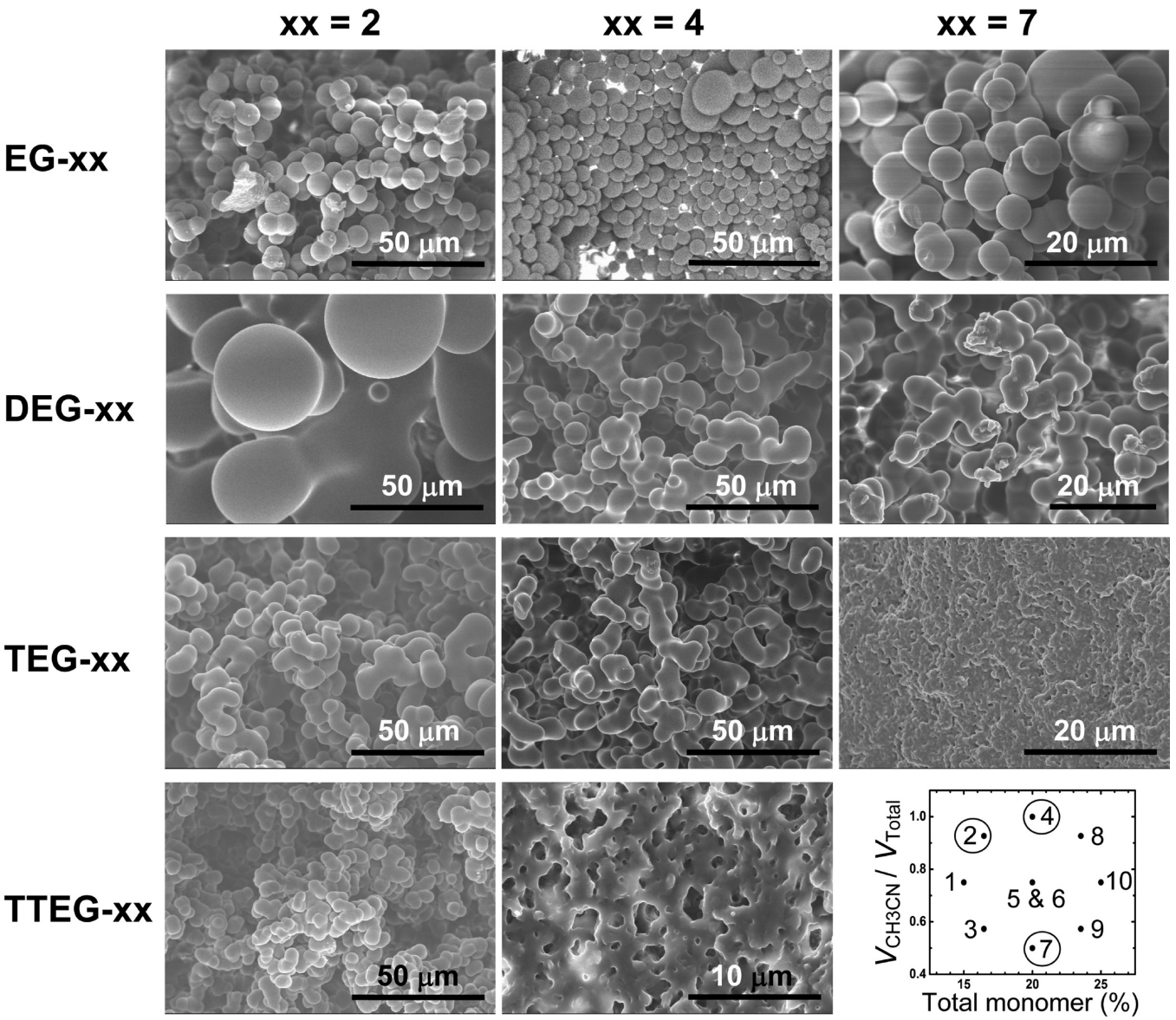

Figure 5. SEM of specific **ALC-xx** samples selected from the domain of the exploratory variables (see lower right frame) for discussion of the growth mechanism of the solid framework (SEMs of all **EG-xx**, **DEG-xx**, and **TEG-xx** samples are shown in Appendix IV of the Supporting Information).

7, **TEG-9**, **TEG-10**, and all **TTEG-xx** samples except **TTEG-2** and **TTEG-4**. Typical DMA data are exemplified with **TEG-8** in Figure 6A. At lower temperatures, all materials were stiff with elastic moduli, G', about 10 times higher than the loss moduli, G''. As temperature increased, both $G'$and G''started decreasing, crossed one another twice, and eventually got again stabilized at higher temperatures. The final values of both $G'$and G'' were about 1000 times lower than their respective low-temperature values, but again G' was approximately 10 times higher than G''. Results from repetitive scans of the same samples were practically identical. The glass transition temperatures reported, T_g, are the maxima of tan δ ($=G''/G'$). T_g values varied randomly by a few degrees within each **ALC-xx**. As shown in Figure 6B, the average T_g values of the four **ALC-xx** followed the order $(T_g)_{EG\text{-}xx} > (T_g)_{DEG\text{-}xx} > (T_g)_{TEG\text{-}xx} > (T_g)_{TTEG\text{-}xx}$ and were spaced approximately 10−20 °C apart from one another (for the primary data refer to Table S.5 in the Supporting Information). The glass transition zones were generally narrow. For instance, all full widths at half maxima (fwhm, Table S.5) of all tan δ plots for all **ALC-xx** were in the range of 12.0−17.7 °C. As the onset of segmental motion in polymers is typically considered the maximum in the G''curve (indicated with an arrow in Figure 6A). Those maxima were generally 10−13 °C lower than the tan δ maxima (see Table S.5 and Figure S.8 in the Supporting Information) and may be considered either as the upper temperature limits for fixing the shape of the polymer or loosely as the onset of shape recovery.

*2.3.2. Elastic Properties of **ALC-xx** under Tension: Strain Recovery, Creep, and Stress Relaxation as a Function of T_g.* As a preamble to the shape memory effect, this section investigates the elastic properties of **ALC-xx** relative to T_g, confirms that **ALC-xx** can store and keep energy (essential for shape recovery), and explores whether they can do that repetitively. This section offers also an insight into the molecular rearrangements associated with settling after the first stretching cycle and in some cases some minor creep afterward. Those results become important in rationalizing differences in shape recovery rates among the various **ALC-xx**.

DOI: 10.1021/acs.chemmater.7b01020
Chem. Mater. 2017, 29, 4461−4477

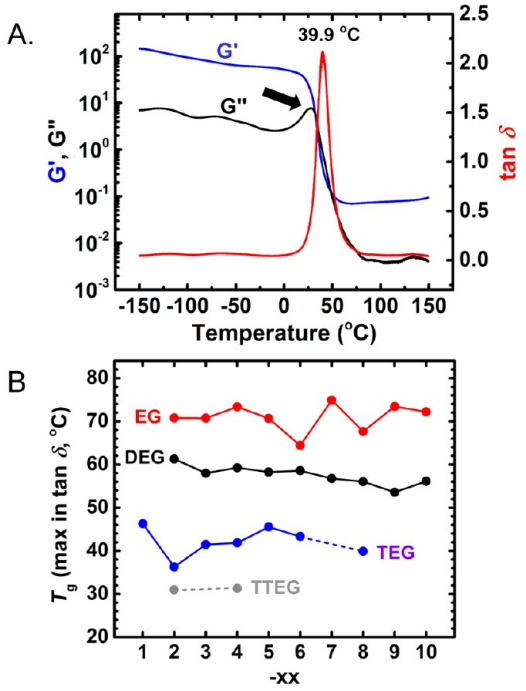

Figure 6. (A) Storage (G') and loss (G'') moduli and tan δ ($=G''/G'$) curves of a representative sample (**TEG-8**) as a function of temperature. Arrow points to the maximum in the G'' curve (see text). (B) Glass transition temperatures (T_g as maxima in tan δ) for all noncollapsed **ALC-xx** (Data from Table S.5 in the Supporting Information).

For those purposes, two randomly selected samples, **DEG-4** and **TEG-8**, were tested under tension at three different temperatures, T_g + 40 °C, T_g, and T_g − 40 °C. That range ensures conditions from well above to well below the glass transition zone (see previous section). Fresh, as-prepared samples were loaded and unloaded five times with constant force ramp rates to predetermined strain values; at the end of the fifth loading cycle, samples were step reloaded to the last strain value, which was maintained while the stress was monitored as a function of time.[72] The ultimate strains at each temperature were set just below the respective failure (snapping) points and chosen (based on preliminary runs) in a way that would accommodate all five cycles (i.e., accounting for creep). The behavior of both **DEG-4** and **TEG-8** was very similar in all aspects. The results with **TEG-8** are shown in Figure 7 (for the results with **DEG-4** see Figure S.9 of Appendix VII in the Supporting Information). Referring to **TEG-8** and Figure 7, at both T_g and T_g + 40 °C (40 and 80 °C, respectively), samples were essentially linearly elastic. Overall, at T_g, samples were about twice as stiff as at T_g + 40 °C. At both temperatures, samples became stiffer at the second loading cycle and beyond (the stress−strain slope increased). Beyond the second cycle, stress−strain curves were superimposable at T_g + 40 °C. At T_g, we noticed a small drift toward larger strains with repetitive cycling (yellow arrow pointing to the right), indicating a small amount of creep. Below the glass transition range (T_g−40 °C = 0 °C), samples were much stiffer (notice the narrow strain range) and repetitive stretching led to accumulation of unrecoverable strains. At T_g + 40 °C samples could store and keep >98% of the energy spent for stretching (last frame of Figure 7). That energy was available for recovery of the original dimensions after stress was released. Energy was progressively lost from the stretched state as the temperature was decreased: already at T_g, **TEG-8** lost about 9% of the energy stored. Below the glass transition range (again at T_g − 40 °C), the energy lost was about 65% and kept on increasing even after 20 min of constant strain. Energy loss notwithstanding, stress relaxation was fast at or above T_g and much slower below the glass transition zone (note the different time scales in the last frame of Figure 7).

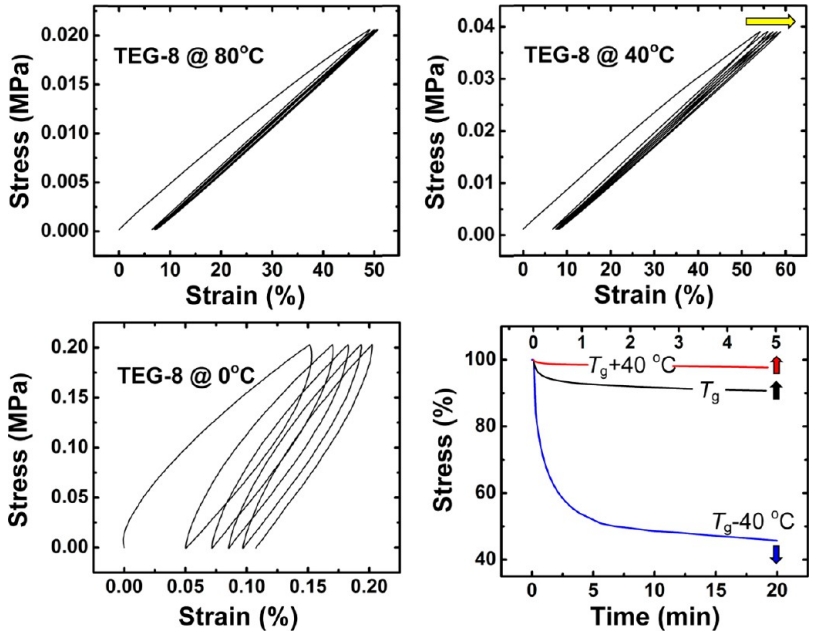

Figure 7. Five consecutive cycle tensile testing of three **TEG-8** samples (one for each frame) at T_g + 40 °C (80 °C), T_g (40 °C), and T_g − 40 °C (0 °C). Samples were stretched with a constant force rate of 1 N min^{-1}. Maximum strains at T_g and T_g + 40 °C were set near the failure point of the sample. Maximum strain at T_g − 40 °C was set by the compliance of the instrument (18 N). Yellow arrow indicates creep. Last frame: Stress relaxation run after at the end of the fifth cycle of each frame.

DOI: 10.1021/acs.chemmater.7b01020
Chem. Mater. 2017, 29, 4461−4477

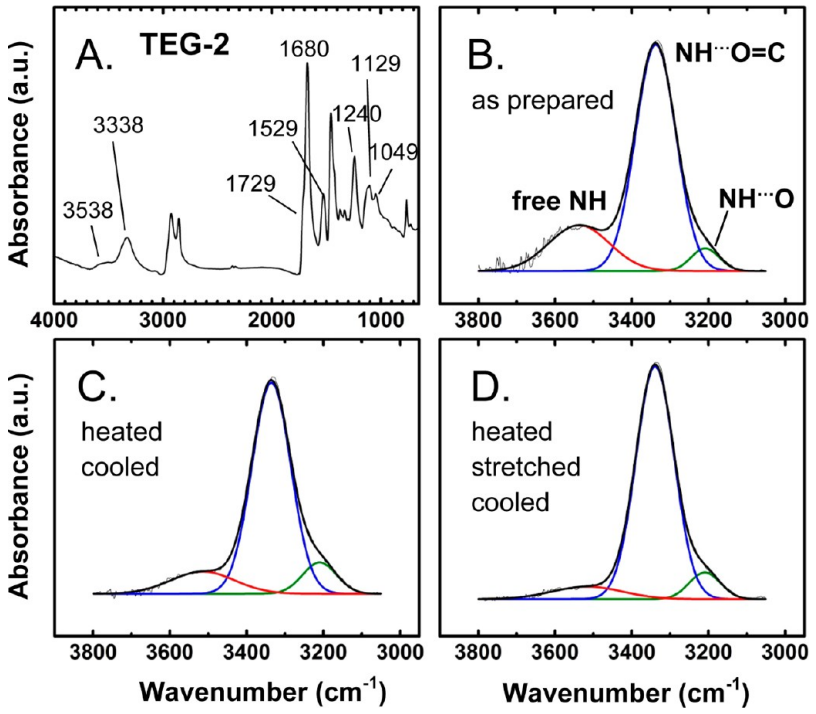

Figure 8. Room-temperature ATR-FTIR spectra of **ALC-xx** taken under different conditions. (A) Entire spectrum of a representative as-prepared **TEG-2** sample. (B) 3000−3800 cm^{-1} range of frame A, deconvoluted for H-bonding. (C) Same sample as in A and B, heated at T_g + 10 °C for 15 min, and then cooled back to room temperature. (D) Same sample as in A−C, heated again at T_g + 10 °C for 15 min, and stretched to about 60% strain; then the stretching force was released, and the sample was let cool back to room temperature (Similar spectra for **DEG-2**, **DEG-4**, **TEG-2**, **TEG-8**, and **TTEG-2** are shown in Appendix V of the Supporting Information. H-bonding data for all samples are summarized in Table 1.).

Table 1. Integrated Ratios of Free and H-Bonded NH Stretching of Samples as Shown[a]

sample	conditions	[free NH] 3423−3545 cm^{-1}	[NH···O=C] 3331−3341 cm^{-1}	[NH···O$(CH_2)_2$] 3204−3234 cm^{-1}
DEG-2	as prepared	4.6	4.4	1.0
	heated−cooled[b]	1.6	7.1	1.3
	heated−stretched−cooled[c]	0.8	7.4	1.8
DEG-4	as prepared	5.5	1.9	1.7
	heated−cooled[b]	1.2	7.6	1.3
	heated−stretched−cooled[c]	0.0	8.6	1.4
TEG-2	as prepared	2.2	7.3	0.5
	heated−cooled[b]	0.8	8.4	0.8
	heated−stretched−cooled[c]	1.3	7.7	1.0
TEG-8	as prepared	2.4	6.6	1.0
	heated−cooled[b]	1.0	7.3	1.7
	heated−stretched−cooled[c]	1.7	6.8	1.5
TTEG-2	as prepared	2.2	6.7	1.1
	heated−cooled[b]	0.0	8.2	1.8
	heated−stretched−cooled[c]	1.1	7.6	1.3

[a]All spectra were taken at room temperature. Data from spectra shown in Figure 8 and Figures S.4-S.7 in the Supporting Information. [b]Heated at T_g + 40 °C, cooled to room temperature. [c]Heated at T_g + 40 °C, stretched at that temperature, left to relax, and cooled back to room temperature.

There are two possible contributors to settling after the first stretching cycle at T_g and T_g + 40 °C or the subsequent creep at T_g: heating, stretching, or both. Insight was obtained with ATR-FTIR of several random **ALC-xx** samples. Spectra of a representative sample (**TEG-2**) are shown in Figure 8 (for the others refer to Appendix V in the Supporting Information). Data relevant to this discussion are summarized in Table 1. All spectra were dominated by the isocyanurate carbonyl stretch near 1680 cm^{-1}. The 2300−2000 cm^{-1} region was clean of any unreacted N=C=O stretch, in agreement with the solid-state NMR data (Figure 2). The free urethane carbonyl stretch was observed at 1729 cm^{-1} as a shoulder to the intense isocyanurate absorption. Possible absorptions of H-bonded urethane carbonyl groups would appear at lower energies, but they were masked by the intense isocyanurate absorption. The N−H bending coupled to C−N stretching gave an absorption at 1529 cm^{-1}.[73] The absorptions at 1240, 1129, and 1049 cm^{-1} were attributed to the ethylene glycol and urethane asymmetric and symmetric C−O−C stretches.[74,75] Using flat baselines from 3050 to 3800 cm^{-1}, the N−H stretch region of all the **ALC-xx** tested was deconvoluted into three absorptions (Figure 8B): one in the 3423−3545 cm^{-1} range (free NH);[76,77] a second one, typically the most intense absorption, in the 3331−3341 cm^{-1} range (NH bonded to carbonyl: NH···O=C);[77,78] and, a

DOI: 10.1021/acs.chemmater.7b01020
Chem. Mater. 2017, 29, 4461−4477

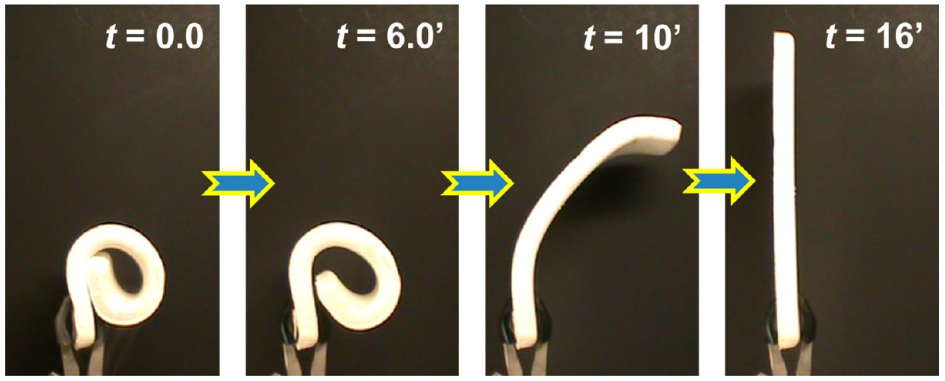

Figure 9. Deployable, shape memory aerogel panel similar to that in Figure 1 (**TEG-8**). The permanent shape was flat. Sample (2" × 8" × 0.4") was heated up above T_g, folded as shown in the first frame, and dipped in liquid N_2. Unfolding to the original shape as the sample returned to room temperature is shown in Movie S.2 of the Supporting Information. Selected frames from that movie are shown here.

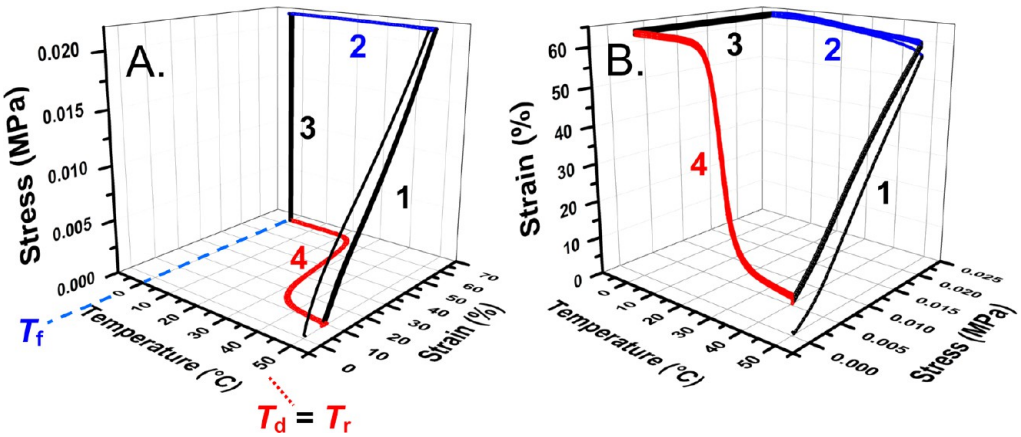

Figure 10. Three-dimensional representation from two different perspectives of a representative temperature cycle experiment aiming at quantifying the figures of merit for the shape memory effect. Data shown are for **TEG-8**. All experiments were performed starting with as-prepared samples, cycled 5 times between a deformation (and recovery) temperature T_d (T_r) and a fixing temperature (T_f). The different stages of the experiment (marked with numbers) are explained in the text.

third weaker absorption in the 3204−3234 cm^{-1} range assigned to NH···$O(CH_2)_2$ (NH stretch, H-bonded to glycol groups).[77,79,80] Following the same trend with the progressive broadening of the −NH(C═O)O− resonance in the ^{13}C NMR spectra and the −NH(C═O)O− resonance in the ^{15}N NMR spectra, it is noted that by going from **DEG-2** to **TEG-2** to **TTEG-2**, the absorption intensity ratio of [free NH]:[NH···O═C]:[NH···$O(CH_2)_2$] moved from 4.6/4.4/1.0 to 2.2/7.3/0.5 to 2.2/6.7/1.1, respectively, showing, albeit only qualitatively,[81] an increase of H-bonded NH at the expense of free NH as the length of the ALC increased.

Now, as demonstrated in Figure 8C, a heating cycle above T_g followed by cooling back to room temperature increased the fraction of H-bonded NH. As summarized in Table 1, the new intensity ratio [free NH]:[NH···O═C]:[NH···$O(CH_2)_2$] moved in favor of NH···O═C, at the expense of free NH, becoming 1.6/7.1/1.3, 0.8/8.4/0.8, and 0.0/8.2/1.8, in **DEG-2**, **TEG-2**, and **TTEG-2**, respectively. Next, we investigated the effect of heating above T_g, stretching at that temperature, and cooling back to room temperature (Figure 8D). That cycle had a similar effect to just heating and cooling; the difference was that a higher portion of free NH would survive the cycle as the ALC became longer (i.e., from DEG to TTEG). The ratio of [free NH]:[NH···O═C]:[NH···$O(CH_2)_2$] for the three **DEG-2**, **TEG-2**, and **TTEG-2** moved to 0.8/7.4/1.8, 1.3/7.7/1.0, and 1.1/7.6/1.3, respectively (Table 1). Similar trends were observed for **DEG-4** and **TEG-8** (data also included in Table 1). In summary, ATR-FTIR data have shown that as-prepared **ALC-xx** were in a metastable state. Both heating and stretching were responsible for settling at energy minima that maximized H-bonding interactions. That provides a satisfactory reason for the stiffness increase noted during the first cycle of tensile testing and the small amount of creep afterward.

2.3.3. Shape Memory Effect (SME). The SME of **ALC-xx** was demonstrated as shown in Figure 9 with a panel similar to the one used in Figure 1 (**TEG-8**). The strain imposed during bending in Figure 1 was about 25% (calculated from the radius of curvature, R, and the thickness of the specimen, d, via d/2R). In order to force strains closer to the ultimate strain of that kind of samples (about 60%; see Figure 7), the sample was folded to the tighter radius of curvature as shown in Figure 9. Thus, first, the panel was heated in an oven at T_g + 40 °C; then it was folded quickly into the spiral form of Figure 9, and that shape was fixed by dipping the folded object in liquid N_2. As the spiral form was let to warm up to ambient temperature, it unfolded to its original shape.

The SME was quantified formally for all noncollapsed **DEG-xx** and **TEG-xx** samples as well as **TTEG-2** and **TTEG-4** via three individual figures of merit (the strain fixity, the strain recovery, and the strain recovery rate) and a cumulative one

DOI: 10.1021/acs.chemmater.7b01020
Chem. Mater. 2017, 29, 4461−4477

(the fill factor). Those figures of merit were calculated from tensile testing data derived from five temperature−stretch−relaxation cycles as demonstrated in Figure 10 (for clarity, the 3D graph is shown from two perspectives).[82] All first cycles started with fresh, as-prepared samples. In Stage 1, samples were first equilibrated for 5 min at their deformation temperatures ($T_d = T_g + 10$ °C) and then stretched at 1 N min^{-1} near to their stretch limit (typically around 60% strain). In Stage 2 (blue line), stress was kept constant at the maximum value attained in Stage 1 and samples were cooled at 5 °C min^{-1} to their fixation temperature (T_f, well below T_g), where they were allowed to equilibrate for 5 min. In Stage 3, the tensile force was decreased to 0.01 N (i.e., stress was practically removed), samples were allowed to relax (fix) isothermally at T_f for 15 min, and the strain was recorded for the duration. Finally, in Stage 4, strain was recorded while samples were heated at 1 °C min^{-1} (red lines) to their recovery temperatures ($T_r = T_d = T_g + 10$ °C). Cycle 2 and subsequent cycles started after an isothermal hold at T_d for 15 min. As expected from the stress−strain curves of Figure 7, all four stages of the thermal cycle curves coincided almost precisely in cycle 2 and above, pointing to a robust SME.

In order to calculate the SME figures of merit, the thermal cycles of Figure 10 were transformed and projected to selected faces of the 3D representations, as follows. First, since the temperature was cycled at fixed rates, each point along the 3D curve is uniquely defined by time. Figure 11A and 11B gives such unfolded-in-time projections of the 3D curves to the strain−temperature (bottom) plane of Figure 10A or equivalently to the rear plane of Figure 10B. Figure 11A shows the strain along a random temperature cycle (after the first), while Figure 11B shows the strain during the first two cycles. Figure 11C is the direct projection (no time unfolding) from the perspective of Figure 10B of one full random cycle to the strain−temperature (rear) plane. All figures of merit of all samples over all cycles are summarized in Table S.6 of Appendix VIII in the Supporting Information. In graph form, results from the first and fifth cycles are shown in Figure 12.

The strain fixity ratio, $R_f(N)$, quantifies creep during Stage 2 (i.e., during cooling under constant stress) and was calculated for each cycle, N, from the data like those of Figure 11A via eq 2.

$$R_f(N) = \frac{\varepsilon_u(N)}{\varepsilon_m(N)} \times 100 \tag{2}$$

(The definitions of the two strain values, ε_u and ε_m, are given directly in Figure 11A.) In agreement with Figure 7, whereas above T_g there is virtually no creep, by and large, strain fixity in all cycles, including the first one, was always >98% (Table S.6.1).

The strain recovery ratio, $R_r(N)$, quantifies fatigue from repetitive cycling, and just like $R_f(N)$, it was also calculated from the data of Figure 11A using eq 3.

$$R_r(N) = \frac{\varepsilon_m(N) - \varepsilon_p(N)}{\varepsilon_m(N)} \times 100 \tag{3}$$

Reflecting the increase in stiffness observed after the first cycle, all strain recovery values started lower in the first cycle (80−90%), increasing and stabilizing thereafter to values 98%. (The increase of $R_r(N)$ beyond the first cycle is already evident from the data shown in Figure 12 but for the near-stabilization just after $N \geq 2$, refer to Table S.6.2.)

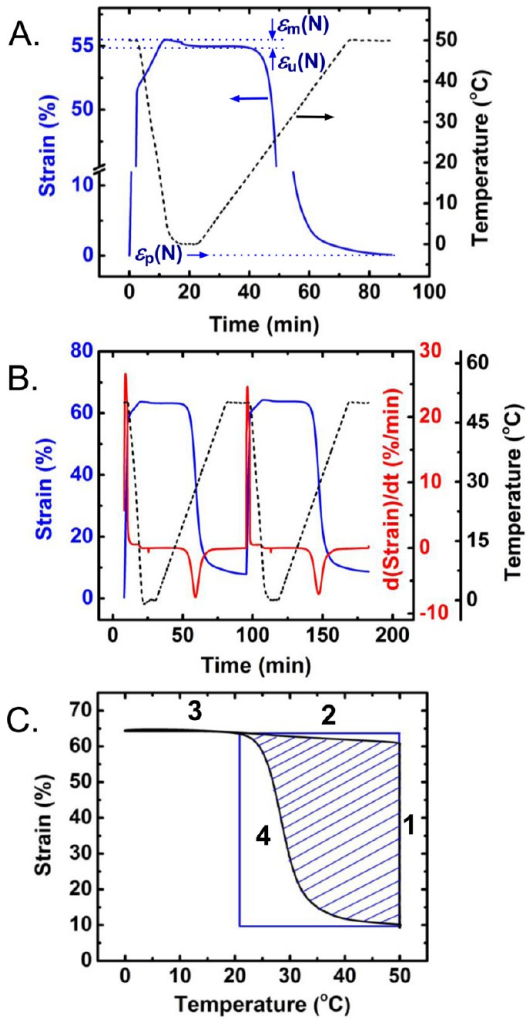

Figure 11. Projections of the entire 3D representation of Figure 10 to different planes in order to calculate the figures of merit of the shape memory effect. (A) Projection to the strain−temperature plane followed by unfolding temperature into time. (Temperature vs time is also included as a dotted line. Strains ε_m, ε_u, and ε_p are used in eqs 2 and 3 and are defined within this frame.) (B) Plotting same as frame A. This frame also includes (red line) a plot of the first derivative of strain over time. (C) Straight projection of the curve to the strain vs temperature plane. Numbers 1−4 refer to the four stages of the experiment as shown in Figure 10.

The strain recovery rate, $R_t(N)$, is an index introduced in this study in order to quantify and compare the relative speed of strain recovery at the heating Stage 4 among different samples and cycles. $R_t(N)$ is defined via eq 4 as the maximum slope of the strain vs time curve during heating in Stage 4 (refer to the red line in Figure 11B).

$$R_t(N) = \max\left[-\frac{d\text{Strain}}{dt}\right] \tag{4}$$

Since the strain recovery of Stage 4 did not take place at the natural warm-up rate of the material but instead was driven by the imposed heating rate, it was deemed necessary to repeat the experiment at different heating rates (using fresh samples each time) and observe the effect on the rate of recovery (Figure 13). Thus, it is noted that during all cycles, $R_t(N)$ followed a near-linear relationship with a heating rate up to 5 °C min^{-1}; therefore, different $R_t(N)$ values reflected steeper recovery

DOI: 10.1021/acs.chemmater.7b01020
Chem. Mater. 2017, 29, 4461−4477

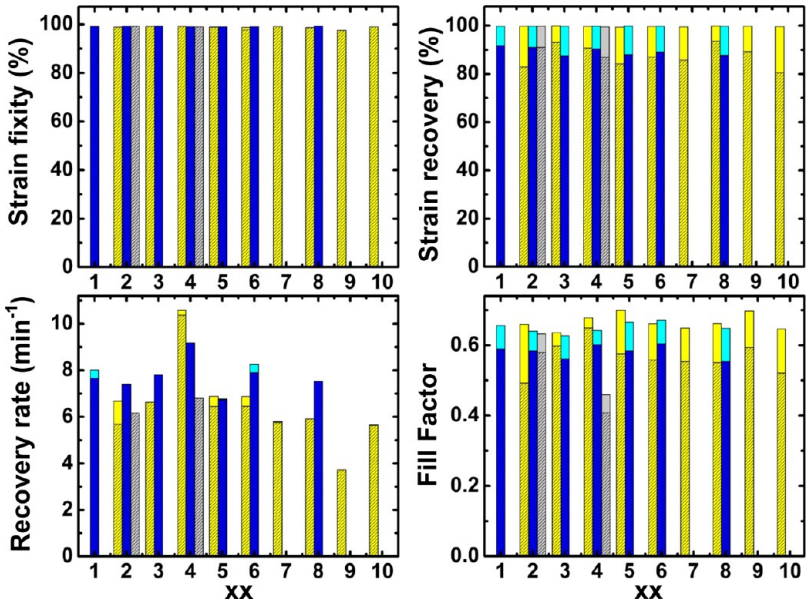

Figure 12. Figures of merit extracted from the data of Figure 11 as described in the text. Color coding: Yellow, **DEG-xx**; blue, **TEG-xx**; gray, **TTEG-xx** (just two samples). Dark or shaded colors: first-cycle data. Lighter colors: fifth-cycle data. (All original data for all samples, and all cycles are summarized in Table S.6 of Appendix VIII in the Supporting Information.).

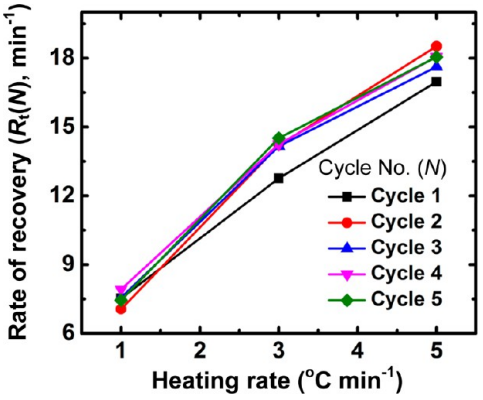

Figure 13. Strain recovery rates, $R_t(N)$, demonstrated with three fresh **TEG-8** samples cycled five times ($1 \leq N \leq 5$) using different heating rates during Stage 4 (i.e., during heating from T_f to T_d; refer to Figures 10 and 11C).

curves or equivalently more narrow temperature windows of recovery. The obvious place to look for supporting evidence for that conclusion was the width of the tan δ plots, but we were unable to find any meaningful correlation between $R_t(N)$ (from Table S.6.3) and the fwhm of tan δ (from Table S.5). Thereby, we concluded that the stretched, frozen starting point of the shape recovery (Stage 4) represented a different state of **ALC-xx** from the as-prepared samples. According to Table 1, that state was most probably characterized by an enhanced amount of H-bonding relative to the innate (as prepared) state of **ALC-*xx***. In that regard, it is worth nothing that the highest recovery rate was observed with **DEG-4**, which, based on the IR data of Table 1, did not show any free NH after one heating–stretching cycle.

Finally, the fill factor, *FF(N)*, has been proposed as a combined index of performance[83] and was calculated from the ratio of the shaded S-shaped area to the total area of the "box" shown in Figure 11C. Obviously, calculation of that ratio is sensitive to the upper and lower temperature limits. As a conservative upper limit we took the maximum temperature for all experiments, T_g + 10 °C (against the recommended T_g + 20 °C). The selection of the lower limit, namely, the onset of recovery (Stage 4), was based on $R_t(N)$ as follows: first, we noted the temperature of the maximum slope (eq 4) of the corresponding Figure 11B of every **ALC-xx** in every cycle; then we located the temperature at the foot of Stage 4 where the recovery rate was at just 3% of the maximum rate. That temperature was set as the onset of recovery in every Figure 11C corresponding to every **ALC-xx** in every cycle. By its construction, *FF(N)* combines contributions from all three $R_f(N)$, $R_r(N)$, and $R_t(N)$ and was also monitored and recorded for all samples during all five cycles. Fill factors (Figure 12, Table S.6.4) started lower in the first cycle but generally no lower than 0.5 (except for **TTEG-4**, where $FF(1) = 0.4$). After samples were broken in in their first cycles, all fill factors were over 0.60, most over 0.65, and in some cases reached 0.70. Those fill factors are in the range for high-speed elastomers and are considered high.[83,84]

Overall, the strategy of using poly(isocyanurate-urethane) aerogels as lightweight alternative to shape memory polymers has been fruitful, leading to materials showing a robust shape memory effect. According to Figure 9, **ALC-xx** can very well serve as deployable panels in applications where weight is at a premium, e.g., as mirrors or antennas in space. Figure 14 shows that **ALC-xx** can also be molded into complex shapes and programmed to perform more advanced functions mimicking, for example, the complicated muscle coordination of a human hand holding a pen. The slow recovery reported in Figure 14 should not be considered as a deterrent. In practice, fast recovery will be driven by heating with a thin wire resistor embedded within an object.

3. CONCLUSION

As a polymeric class, polyisocyanurates have received a low level of attention as base materials for polymeric aerogels. As shown here though, the isocyanurate ring can be an effective cross-linking node for imparting both rubber-like elasticity and

DOI: 10.1021/acs.chemmater.7b01020
Chem. Mater. 2017, 29, 4461–4477

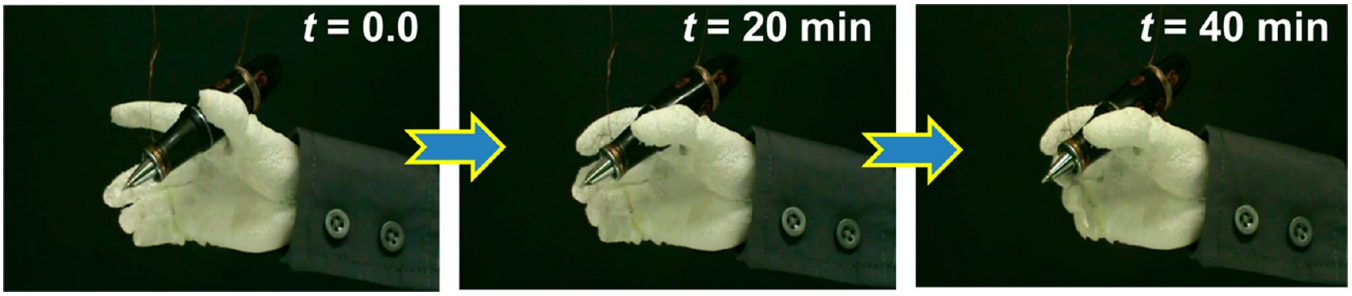

Figure 14. Bionic hand based on a shape memory polyurethane aerogel (**TEG-8**). In its permanent shape (last frame to the right) the "hand" had been programmed to hold a pen. Frames are taken from Movie S.3 of the Supporting Information. All other conditions are identical to those of Figure 9.

insolubility of a developing polyurethane network. Both are necessary conditions for the shape memory effect and the synthesis of polymeric aerogels, respectively. Given the specific triisocyanurate node used in this work (a hexamethylene diisocyanate derivative), longer diols (selected from the ethylene glycol family) and solvents with enhanced H-bonding ability (like acetone) lead to extensive shrinkage and dense polymers; thereby, they were not suitable for shape memory aerogel synthesis. Once the correct conditions were identified with the help of design-of-experiments statistical methods, poly(isocyanurate-urethane) aerogels showed a robust shape memory effect with high fixity and recovery ratios and fill factors. Since aerogels are low-density materials, large-scale applications of shape memory polymers, as in deployable panels and biomimetic devices, are becoming amount-of-material efficient and within reach. Owing to the necessary compromise between conflicting requirements for rubber-like superelasticity and particle network formation, the aerogel framework of **ACL-xx** consisted of large particles (by aerogel standards). As represented in the Introduction, aerogels with nanostructures consisting of large particles may not be suitable for typical aerogel applications like in thermal insulation. Nevertheless, preliminary results show that the room-temperature thermal conductivity of several **ALC-xx** selected randomly was in the 0.052 ± 0.005 W m^{-1} K^{-1} range, namely, similar to several commercial thermal insulators like glass or rock wool. Interestingly, filling the pores of **ALC-xx** with silica aerogel (0.015 W m^{-1} K^{-1}) caused a drop of the thermal conductivity to around 0.027 W m^{-1} K^{-1}, namely, within a range accessible mainly by aerogels. The properties of those composites are under further investigation.

4. EXPERIMENTAL SECTION

4.1. Materials. All reagents and solvents were used as received unless noted otherwise. The isocyanurate node (N3300A) was obtained courtesy of Covestro LLC (Pittsburgh, PA) under the trade name Desmodur N3300A. Diols (ALC) (ethylene glycol (EG), diethylene glycol (DEG), triethylene glycol (TEG), tetraethylene glycol (TTEG)), the catalyst (dibutyltin dilaurate (DBTDL)), and solvents (anhydrous acetonitrile and anhydrous acetone) were purchased from Sigma-Aldrich. Siphon-grade CO_2 was purchased from Ozark Gas Co.

4.2. Synthesis of Shape Memory Poly(isocyanurate-urethane) Aerogels. In a typical process, N3300A as received (Desmodur N3300A, 0.504 g, 1.00 mmol) and the respective diol (EG, DEG, TEG, and TTEG, 1.50 mmol) were dissolved in an anhydrous acetonitrile/acetone mixture according to a central composite rotatory design (CCRD) model (Appendix I in Supporting Information). The solution was stirred in a three-neck round-bottom flask at 23 °C under N_2 for 10 min, and DBTDL (5 μL) was added. The resulting sol was stirred for another 5 min and poured into molds. Smaller rectangular specimens for dynamic mechanical analysis were cut from cylindrical samples prepared using plastic syringes as molds (All Plastic Norm-Ject Syringes, 20 mL, Fisher Scientific Catalogue No. 14-817-32, 2.53 cm i.d.). Larger rectangular samples (e.g., Figures 1 and 9) were prepared using plastic containers (Style Selections 16" × 12.75" Plastic Multi-Use Insert Drawer Organizer, Model No. 39001, Lowe's Item No. 105922). Molds for bionic hands (Figure 14) were prepared via a 3-stage process: first, the negative of a volunteer's hand was reproduced into Alja-Safe (Crystalline Silica-Free Alginate for Molding Body Parts);[85] plaster (DAP 4-lb Carton Plaster of Paris Model 10318, Lowe's Item No. 41323) was cast into the alginate mold in order to produce the exact (positive) replica of the hand; finally, the plaster mold was used to make the final mold using AeroMarine Products AM 128 Silicone Mold Making Rubber RTV.[86] Molds with sol were sealed with Parafilm and kept at room temperature for gelation. The gelation time varied from 7 min to about 3 h 40 min depending on the chemical identity of the alcohol, the monomer concentration, and the fraction of CH_3CN in the solvent system. Gels were aged for 24 h in their molds at room temperature. Subsequently, gels were removed from the molds, washed with acetone (4 × 8 h, using 4× the volume of the gel each time), and dried with CO_2 taken out as a supercritical fluid (SCF). Samples are referred to as **ALC-xx**, where **ALC** stands for the abbreviation of the diol (Scheme 1) and **xx** denotes the position in the domain of the independent variables domain (Scheme 2B).

4.3. Methods. *4.3.1. Drying.* Drying of wet-gels was carried out in an autoclave (SPIDRY Jumbo Supercritical Point Dryer, SPI Supplies, Inc. West Chester, PA, or a Spe-edSFE system, Applied Separations, Allentown, PA). Samples were loaded into the autoclave at room temperature and covered with acetone. The pressure vessel was closed, and liquid CO_2 was allowed in at room temperature. Acetone was drained out from the pressure vessel while more liquid CO_2 was allowed in. Samples were kept under liquid CO_2 for 30 min. Then liquid CO_2 was drained out while more liquid CO_2 was allowed in. The cycle was repeated several times until all acetone had been extracted out of the pores of the samples. Subsequently, the temperature of the autoclave was raised to 40 °C, and that condition was maintained for 1 h. Finally, supercritical fluid (SCF) CO_2 was vented off as a gas.

4.3.2. Chemical Characterization. Solid-state CPMAS ^{13}C NMR spectra were obtained with samples cut into small pieces on a Bruker Avance III 400 MHz spectrometer with a carbon frequency of 100 MHz using a 7 mm Bruker MAS probe at a magic angle spinning rate of 5 kHz with broad-band proton suppression and the CP TOSS pulse sequence. The Total Suppression of Spinning Sidebands (TOSS) pulse sequence was applied by using a series of four properly timed 180° pulses on the carbon channel at different points of a cycle before acquisition of the FID, after an initial excitation with a 90° pulse on the proton channel. The 90° excitation pulse on the proton and the 180° excitation pulse on carbon were set to 4.2 and 10 μs, respectively. A contact time of 2 ms was used for cross-polarization. Solid-state ^{13}C NMR spectra were referenced externally to glycine (carbonyl carbon at 176.03 ppm). Chemical shifts are reported versus TMS (0 ppm).

DOI: 10.1021/acs.chemmater.7b01020
Chem. Mater. 2017, 29, 4461−4477

Solid-state CPMAS ^{15}N NMR spectra were also obtained on the same Bruker Avance III 400 MHz Spectrometer with a nitrogen frequency of 40.557 MHz using a 7 mm Bruker MAS probe with broad-band proton suppression and magic angle spinning rate of 5 kHz. For cross-polarization, a 90° proton excitation pulse was set to 4.2 μs with 2 ms contact time. Chemical shifts are reported versus liquid ammonia (0 ppm) and were externally referenced to glycine (amine nitrogen at 33.40 ppm). In all solid-state NMR experiments the relaxation delay was set at 5 s.

Attenuated total reflectance (ATR) FTIR spectroscopy was carried out with a Nicolet-FTIR spectrometer model 750, equipped with a ATR accessory model 0012-3XXT. Samples were cut to the size of the ATR crystal (ZnSe, rectangular, 20 mm × 50 mm), and ATR-FTIR spectra were obtained by pressing them against the crystal with the ATR unit's pressure device (gripper). Maximum throughput of the infrared beam to the detector was achieved via optical alignment that was performed with no sample on the crystal. Data were collected at an incident beam angle of 45° over 32 scans with a resolution of 2 cm^{-1}. In the ATR mode, the penetration depth (pd) and thereby the effective path length (=number of reflections × pd) of the infrared beam are directly proportional to the wavelength. Thereby, an ATR correction was applied to the raw data by multiplying the spectra with a wavelength-dependent factor (roughly $\lambda/5$) that adjusts the relative peak intensities. In order to evaluate H-bonding, the ν(N−H) bands were deconvoluted into three Gaussian-shaped peaks. Peak curve fitting was performed using the Origin 8.5 software package.

4.3.3. Physical Characterization. Bulk densities (ρ_b) were calculated from the weight and the physical dimensions of the samples. Skeletal densities (ρ_s) were determined with helium pycnometry using a Micromeritics AccuPyc II 1340 instrument.

4.3.4. Structural Characterization. Structural characterization was carried out using scanning electron microscopy (SEM) with Au-coated samples on a Hitachi model S-4700 field-emission microscope.

4.3.5. Thermomechanical Characterization. Thermomechanical characterization was carried out in the tension mode with a TA Instruments Q800 Dynamic Mechanical Analyzer (DMA) equipped with a tension clamp (TA Instruments part no. 984016.901). All specimens for testing had a rectangular geometry (length 20 mm; width 15 mm; thickness 3−4 mm) in the spirit of ASTM D790-10[87] and ASTM D4065;[88] they were cut off with a knife under N_2 in a glovebox, from larger cylindrical samples dipped in liquid N_2. In order to ensure uniform thickness, the surface of all rectangular pieces was smoothened, while still frozen, with a 3 M sand paper (320 grit, part no. 98401). In general, all samples were placed in the load cell at room temperature. The exact length of all samples was measured by the instrument under a small tensile force (0.01 N) that prevents bending. The temperature was stepped to the initial testing temperature, and samples were equilibrated at that temperature for 5 min.

Glass transition temperatures (T_g) were extracted from the viscoelastic properties of the samples, which were measured by applying a continuous sinusoidal oscillation (1 Hz) with a strain amplitude equal to 0.3%, while the temperature was ramped from −150 to 150 °C at 3 °C min^{-1}.

Strain recovery (creep) and stress relaxation experiments were carried out at three different temperatures (T_g + 40 °C, T_g, and T_g − 40 °C) with two samples selected among those with the highest fill factors (**DEG-4** and **TEG-8**). For this, each sample was first stepped and then equilibrated at the particular temperature for 5 min. Subsequently, samples were stretched with a small tensile force (0.01 N), and the length of the sample was measured by the instrument and stored. Each strain recovery cycle began with a deformation stage wherein the sample was stretched at a constant force rate of 1 N min^{-1} up to a final strain and then the force was released again at 1 N min^{-1}. At T_g and T_g + 40 °C, the final strain was about 50% (i.e., near the sample break point); at T_g−40 °C, the final strain was determined by the compliance of the instrument (18 N) and was about 2−4% for **DEG-4** and 0.1% for **TEG-8**. That stress−release cycle was repeated at each temperature five times. After the end of the fifth cycle, the sample was step stretched to the final strain reached at the fifth cycle, and that strain was maintained for 20 min while the residual force with which the sample pulls the clamps together was recorded as a function of time.

Shape memory-related properties (strain fixity, strain recovery, strain recovery rates, and fill factors) were studied in the controlled force mode as follows: samples were first stepped and then equilibrated at their deformation temperature ($T_d = T_g$ + 10 °C) for 5 min. Subsequently, samples were stretched with a small tensile force (0.01 N), and the length of the sample was measured by the instrument and stored. Next, specimens were stretched at a constant force rate of 1 N min^{-1} up to a little below their break point (typically around 60% strain), and then they were cooled, while under the final stress, at 5 °C min^{-1} to their fixation temperature ($T_f \ll T_g$). At that point (T_f), samples were equilibrated for 5 min, and the tensile force was reduced to 0.01 N. Samples were allowed to relax (fix) for 15 min (always at T_f) while strain was recorded. Finally, samples were heated at 1 °C min^{-1} to their recovery temperature ($T_r = T_d$) while strain was still recorded. (As a control, a sample was also heated at 3 °C min^{-1} as well as at 5 °C min^{-1}.) Samples were held at T_d of 15 min, and the cycle was repeated. Five such cycles were run successively for each sample, and data were analyzed for the fixation and recovery properties.

■ ASSOCIATED CONTENT

Supporting Information

The Supporting Information is available free of charge on the ACS Publications website at DOI: 10.1021/acs.chemmater.7b01020.

Appendix I (Design, formulation, and gelation times of **ALC-xx**); Appendix II (General material properties of **ALC-xx**); Appendix III (Fitting bulk densities of **ALC-xx** to system variables); Appendix IV (SEM of all **ALC-xx**); Appendix V (ATR-FTIR of **DEG-2**, **DEG-4**, **TEG-8**, and **TTEG-2**); Appendix VI (Glass transition data); Appendix VII (Tensile testing and stress relaxation of **DEG-4**); Appendix VIII (Figures of merit for the SME of all **ALC-xx**) (PDF)

Movie of a demonstration of superelasticity (MPG)

Movie of a demonstration of a deployable panel (MPG)

Movie of a bionic hand (MPG)

■ AUTHOR INFORMATION

Corresponding Authors

*Phone: 573-341-4391. E-mail: leventis@mst.edu.

*Phone: 573-341-4353. E-mail: cslevent@mst.edu.

ORCID

Nicholas Leventis: 0000-0002-7575-9498

Notes

The authors declare no competing financial interest.

†T.L. and J.S.: Summer students via the ARO High School Student Apprenticeship Program.

■ ACKNOWLEDGMENTS

We thank the Army Research Office for financial support under Award Number W911NF-14-1-0369. We also thank BASF Polyurethanes GmbH for partial support. We also thank Covestro LLC (formerly Bayer Corp. U.S.A.) for the generous supply of Desmodur N3300A and the Materials Research Center of the Missouri University of Science and Technology for support with materials characterization.

■ REFERENCES

(1) Koerner, H.; Price, G.; Pearce, N. A.; Alexander, M.; Vaia, R. A. Remotely Actuated Polymer Nanocomposites—Stress-Recovery of

DOI: 10.1021/acs.chemmater.7b01020
Chem. Mater. 2017, 29, 4461−4477

Carbon-Nanotube-Filled Thermoplastic Elastomers. *Nat. Mater.* **2004**, *3*, 115−120.
(2) Lendlein, A.; Jiang, H. Y.; Junger, O.; Langer, R. Light-Induced Shape-Memory Polymers. *Nature* **2005**, *434*, 879−882.
(3) Choi, W.; Lahiri, I.; Seelaboyina, R.; Kang, Y. S. Synthesis of Graphene and its Applications: A Review. *Crit. Rev. Solid State Mater. Sci.* **2010**, *35*, 52−71.
(4) Kim, H.; Abdala, A. A.; Macosko, C. W. Graphene/Polymer Nanocomposites. *Macromolecules* **2010**, *43*, 6515−6530.
(5) Chen, S. J.; Hu, J. L.; Chen, S. G. Studies of The Moisture-Sensitive Shape Memory Effect of Pyridine-Containing Polyurethanes. *Polym. Int.* **2012**, *61*, 314−320.
(6) Saunders, J. H.; Frisch, K. C. *Polyurethane Chemistry and Technology I. Chemistry*; Interscience Publishers: New York, 1962.
(7) Sokolowski, W. M.; Tan, S. C. Advanced Self-Deployable Structures for Space Applications. *J. Spacecr. Rockets* **2007**, *44*, 750−754.
(8) Metzger, M. F.; Wilson, T. S.; Schumann, D.; Matthews, D. L.; Maitland, D. J. Mechanical Properties of Mechanical Actuator for Treating Ischemic Stroke. *Biomed. Microdevices* **2002**, *4*, 89−96.
(9) Daniels, A. U.; Chang, M. K.; Andriano, K. P.; Heller, J. Mechanical Properties of Biodegradable Polymers and Composites Proposed for Internal Fixation of Bone. *J. Appl. Biomater.* **1990**, *1*, 57−78.
(10) Lendlein, A.; Langer, R. Biodegradable, Elastic Shape-Memory Polymers for Potential Biomedical Applications. *Science* **2002**, *296*, 1673−1676.
(11) Metcalfe, A.; Desfaits, A.; Salazkin, I.; Yahia, L. H.; Sokolowski, W. M.; Raymond, J. Cold Hibernated Elastic Memory Foams for Endovascular Interventions. *Biomaterials* **2003**, *24*, 491−497.
(12) Gonzalez-Garcia, Y.; Mol, J. M. C.; Muselle, T.; De Graeve, I.; Van Assche, G.; Scheltjens, G.; Van Mele, B.; Terryn, H. A Combined Mechanical, Microscopic and Local Electrochemical Evaluation of Self-Healing Properties of Shape-Memory Polyurethane Coatings. *Electrochim. Acta* **2011**, *56*, 9619−9626.
(13) Hood, P. J.; Garrigan, S.; Auffinger, F. Method of Making and Using Shape Memory Polymer Patches. U.S. Patent No. 7981229B2, 2011.
(14) Sahoo, N. G.; Jung, Y. C.; Goo, N. S.; Cho, J. W. Conducting Shape Memory Polyurethane-Polypyrrole Composites for An Electroactive Actuator. *Macromol. Mater. Eng.* **2005**, *290*, 1049−1055.
(15) Hu, J. L.; Meng, H. P.; Li, G. Q.; Ibekwe, S. I. A Review of Stimuli-Responsive Polymers for Smart Textile Applications. *Smart Mater. Struct.* **2012**, *21*, 053001.
(16) Mock, C. C. Assembly for Delayed Lowering of a Raised Toilet Seat. U.S. Patent No. 8359677B1, 2013.
(17) Kikutani, T.; Kondo, S.; Hayashi, S.; Sugihara, K.; Haguri, T.; Akimoto, K. Grip Member, Toothbrush Using The Grip Member and Western Tableware Using The Grip Member. U.S. Patent No. 6173477, 2001.
(18) Ölander, A. An Electrochemical Investigation of Solid Cadmium-Gold Alloys. *J. Am. Chem. Soc.* **1932**, *54*, 3819−3833.
(19) Buehler, W. J.; Gilfrich, J. W.; Wiley, R. C. Effects of Low-Temperature Phase Changes on The Mechanical Properties of Alloys Near Composition TiNi. *J. Appl. Phys.* **1963**, *34*, 1475−1477.
(20) Wang, F. E.; Buehler, W. J.; Pickart, S. J. Crystal Structure and a Unique Martensitic Transition of TiNi. *J. Appl. Phys.* **1965**, *36*, 3232−3239.
(21) For an example of superelasticity, see: https://www.youtube.com/watch?v=1rrPv5AlVXg.
(22) Duerig, T. W.; Pelton, A. R. Ti-Ni Shape Memory Alloys. In *Materials Properties Handbook: Titanium Alloys*; Welsch, G., Boyer, R., Collings, E. W., Eds.; American Society for Metals, 1994; pp 1035−1048.
(23) Vernon, L. B.; Vernon, H. M. Producing Molded Articles such as Dentures from Thermoplastic Synthetic Resins. U.S. Patent No. 2234993, 1941.
(24) Rainer, W. C.; Redding, E. M.; Hitov, J. J.; Sloan, A. W.; Stewart, W. D. Heat-Shrinkable Polyethylene. U.S. Patent No. 3144398, 1964.
(25) Perrone, R. J. Heat-shrinkable Articles Made from Silicone Rubber−Polyethylene Compositions. U.S. Patent No. 3326869, 1967.
(26) Wray, C. P. E. Elastic Memory Articles. U.S. Patent No. GB1075704, 1967.
(27) Hayashi, S.; Shirai, Y. Development of Polymeric Shape Memory Material. *Mitsubishi Technical Bulletin 184*; Dec 1988.
(28) Hayashi, S.; Tobushi, H.; Kojima, S. Mechanical Properties of Shape Memory Polymer of Polyurethane Series. *JSME Int. J., Ser. I* **1992**, *35*, 296−302.
(29) Hayashi, S. Properties and Applications of Polyurethane-Series Shape Memory Polymer. *Int. Prog. Urethanes* **1993**, *6*, 90−115.
(30) "Rubber-like elasticity" sometimes is also referred to as a "memory effect", which might become a source of confusion, particularly with respect to SMPs. Used in this context, "memory effect" has nothing to do with shape recovery triggered by an external stimulus.
(31) Berg, G. J.; McBride, M. K.; Wang, C.; Bowman, C. N. New Directions in the Chemistry of Shape Memory Polymers. *Polymer* **2014**, *55*, 5849−5872.
(32) Hager, M. D.; Bode, S.; Weber, C.; Schubert, U. S. Shape Memory Polymers: Past, Present and Future Developments. *Prog. Polym. Sci.* **2015**, *49-50*, 3−33.
(33) Behl, M.; Razzaq, M. Y.; Lendlein, A. Multifunctional Shape-Memory Polymers. *Adv. Mater.* **2010**, *22*, 3388−3410.
(34) Kagami, Y.; Gong, J. P.; Osada, Y. Shape Memory Behaviors of Crosslinked Copolymers Containing Stearyl Acrylate. *Macromol. Rapid Commun.* **1996**, *17*, 539−543.
(35) Hu, J. L.; Mondal, S. Structural Characterization and Mass Transfer Properties of Segmented Polyurethane: Influence of Block Length of Hydrophilic Segments. *Polym. Int.* **2005**, *54*, 764−771.
(36) Pilate, F.; Mincheva, R.; De Winter, J.; Gerbaux, P.; Wu, L.; Todd, R.; Raquez, J. M.; Dubois, P. Design of Multistimuli-Responsive Shape-Memory Polymer Materials by Reactive Extrusion. *Chem. Mater.* **2014**, *26*, 5860−5867.
(37) Zhu, Y.; Hu, J.; Yeung, K. W.; Choi, K. F.; Liu, Y. Q.; Liem, H. M. Effect of Cationic Group Content on Shape Memory Effect in Segmented Polyurethane Cationomer. *J. Appl. Polym. Sci.* **2007**, *103*, 545−556.
(38) Shi, Y.; Yoonessi, M.; Weiss, R. A. High Temperature Shape Memory Polymers. *Macromolecules* **2013**, *46*, 4160−4167.
(39) Xie, T.; Rousseau, I. A. Facile Tailoring of Thermal Transition Temperatures of Epoxy Shape Memory Polymers. *Polymer* **2009**, *50*, 1852−1856.
(40) Nair, D. P.; Cramer, N. B.; Scott, T. F.; Bowman, C. N.; Shandas, R. Photopolymerized Thiol-Ene Systems as Shape Memory Polymers. *Polymer* **2010**, *51*, 4383−4389.
(41) Liu, C. D.; Chun, S. B.; Mather, P. T.; Zheng, L.; Haley, E. H.; Coughlin, E. B. Chemically Cross-Linked Polycyclooctene: Synthesis, Characterization, and Shape Memory Behavior. *Macromolecules* **2002**, *35*, 9868−9874.
(42) Sakurai, K.; Kashiwagi, T.; Takahashi, T. Crystal Structure Of Polynorbornene. *J. Appl. Polym. Sci.* **1993**, *47*, 937−940.
(43) Li, F. K.; Zhu, W.; Zhang, X.; Zhao, C. T.; Xu, M. Shape Memory Effect of Ethylene−Vinyl Acetate Copolymers. *J. Appl. Polym. Sci.* **1999**, *71*, 1063−1070.
(44) Sakurai, K.; Tanaka, H.; Ogawa, N.; Takahashi, T. Shape-Memorizable Styrene-Butadiene Block Copolymer. I. Thermal And Mechanical Behaviors and Structural Change with Deformation. *J. Macromol. Sci., Part B: Phys.* **1997**, *36*, 703−716.
(45) Pierre, A. C.; Pajonk, G. M. Chemistry of Aerogels and Their Applications. *Chem. Rev.* **2002**, *102*, 4243−4265.
(46) Morris, C. A.; Anderson, M. L.; Stroud, R. M.; Merzbacher, C. I.; Rolison, D. R. Silica Sol as A Nanoglue: Flexible Synthesis of Composite Aerogels. *Science* **1999**, *284*, 622−624.
(47) Chidambareswarapattar, C.; McCarver, P. M.; Luo, H.; Lu, H.; Sotiriou-Leventis, C.; Leventis, N. Fractal Multiscale Nanoporous Polyurethanes: Flexible to Extremely Rigid Aerogels from Multifunctional Small Molecules. *Chem. Mater.* **2013**, *25*, 3205−3224.

DOI: 10.1021/acs.chemmater.7b01020
Chem. Mater. 2017, 29, 4461−4477

(48) Chidambareswarapattar, C.; Xu, L.; Sotiriou-leventis, C.; Leventis, N. Robust Monolithic Multiscale Nanoporous Polyimides and Conversion to Isomorphic Carbons. *RSC Adv.* **2013**, *3*, 26459−26469.
(49) Bang, A.; Buback, C.; Sotiriou-Leventis, C.; Leventis, N. Flexible Aerogels from Hyperbranched Polyurethanes: Probing The Role of Molecular Rigidity with Poly(Urethane Acrylates) Versus Poly-(Urethane Norbornenes). *Chem. Mater.* **2014**, *26*, 6979−6993.
(50) Kucheyev, S. O.; Stadermann, M.; Shin, S. J.; Satcher, J. H., Jr.; Gammon, S. A.; Letts, S. A.; van Buuren, T.; Hamza, A. V. Super-Compressibility of Ultralow-Density Nanoporous Silica. *Adv. Mater.* **2012**, *24*, 776−780.
(51) Hayase, G.; Kanamori, K.; Nakanishi, K. New Flexible Aerogels and Xerogels Derived from Methyltrimethoxysilane/Dimethyldimethoxysilane co-Precursors. *J. Mater. Chem.* **2011**, *21*, 17077−17079.
(52) Hayase, G.; Kanamori, K.; Hasegawa, G.; Maeno, A.; Kaji, H.; Nakanishi, K. A Superamphiphobic Macroporous Silicone Monolith with Marshmallow-like Flexibility. *Angew. Chem., Int. Ed.* **2013**, *52*, 10788−10791.
(53) Kanamori, K.; Aizawa, M.; Nakanishi, K.; Hanada, T. New Transparent Methylsilsesquioxane Aerogels and Xerogels with Improved Mechanical Properties. *Adv. Mater.* **2007**, *19*, 1589−1593.
(54) Michal, B. T.; Brenn, W. A.; Nguyen, B. N.; McCorkle, L. S.; Meador, M. A. B.; Rowan, S. J. Thermoresponsive Shape-Memory Aerogels from Thiol-Ene Networks. *Chem. Mater.* **2016**, *28*, 2341−2347.
(55) Meador, M. A. B.; Malow, E. J.; Silva, R.; Wright, S.; Quade, D.; Vivod, S. L.; Guo, H.; Guo, J.; Cakmak, M. Mechanically Strong, Flexible Polyimide Aerogels Cross-Linked with Aromatic Triamine. *ACS Appl. Mater. Interfaces* **2012**, *4*, 536−544.
(56) Leventis, N.; Chidambareswarapattar, C.; Bang, A.; Sotiriou-Leventis, C. Cocoon-in-Web-like Superhydrophobic Aerogels from Hydrophilic Polyurea and Use in Environmental Remediation. *ACS Appl. Mater. Interfaces* **2014**, *6*, 6872−6882.
(57) Chidambareswarapattar, C.; McCarver, P. M.; Luo, H.; Lu, H.; Sotiriou Leventis, C.; Leventis, N. Fractal Multiscale Nanoporous Polyurethanes: Flexible to Extremely Rigid Aerogels from Multifunctional Small Molecules. *Chem. Mater.* **2013**, *25*, 3205−3224.
(58) Skowronski, M. J.; DeLeon, A. Isocyanurate Foam-The Role of the Isocyanate. *Technical Papers-Society of Plastics Engineers* **1977**, *23*, 167−170.
(59) Kordomenos, P. I.; Kresta, J. E.; Frisch, K. C. Thermal Stability of Isocyanate-Based Polymers. 2. Kinetics of Thermal Dissociation of Model Urethane, Oxazolidone, and Isocyanurate Block Copolymers. *Macromolecules* **1987**, *20*, 2077−2083.
(60) Modesti, M.; Simioni, F.; Checchin, M.; Pielichowski, J.; Prociak, A. Thermal Stability and Fire Performance of Modified Polyisocyanurate Foams. *Cell. Polym.* **1999**, *18*, 329−342.
(61) Petunova, M. D.; Luchkina, L. V.; Askadskii, A. A.; Kovriga, O. V. Synthesis and Properties of Poyisocyanurate Networks Based on 2,4-Toluene Diisocyanate and Poly(oxytetramethylene) Glycol. *Polym. Sci., Ser. A* **2009**, *51*, 542−549.
(62) Liszkowska, J.; Czuprynski, B.; Paciorek-Sadowska, J. Thermal Properties of Polyurethane-Polyisocyanurate (PUR-PIR) Foams Modified with Tris(5-hydroxypentyl) Citrate. *J. Adv. Chem. Eng.* **2016**, *6*, 1000148.
(63) Polyurethane and Polyiso: the Difference? PIMA Technical Bulletin #202; http://c.ymcdn.com/sites/www.polyiso.org/resource/resmgr/technical_bulletins/tb202_jun30.pdf (Accessed Jan 18, 2017).
(64) Maleki, H.; Durães, L. Portugal, A. Development of Mechanically Strong Ambient Pressure Dried Silica Aerogels with Optimized Properties. *J. Phys. Chem. C* **2015**, *119*, 7689−7703.
(65) Montgomery, D. C. *Design and Analysis of Experiments*, 6th ed.; John Wiley & Sons: New York, 2006.
(66) Goupy, J.; Creighton, L. *Introduction to Design of Experiments with JMP Examples*, 3rd ed; SAS Institute Inc.: Cary, NC, 2007.
(67) *Using JMP 11*; SAS Institute Inc, Cary, NC, 2013; http://www.jmp.com/en_us/offers/free-trial.html?utm_source=google&utm_campaign=td70114000002KZJq&utm_medium=cpc&utm_term=sas%20jmp (Accessed Jan 25, 2017).
(68) It is noted that in our case (2 exploratory variables) the total number of samples required by the CCRD model (9 plus one repeat at the center) is equal to what would have been required by a fully factorial design (FFD) model using two exploratory variables at three levels each. The difference between FFD and CCRD is that in the latter all peripheral points are equidistant from the center point of the domain.
(69) Mohite, D. P.; Mahadik-Khanolkar, S.; Luo, H.; Lu, H.; Sotiriou-Leventis, C.; Leventis, C. Polydicyclopentadiene Aerogels Grafted with PMMA: II. Nanoscopic Characterization and Origin of Macroscopic Deformation. *Soft Matter* **2013**, *9*, 1531−1539.
(70) Porosities, π, were calculated via $\pi = (\rho_s - \rho_b)/\rho_s$, whereas skeletal densities—ρ_s, included in Table S.3—were for all **ALC-*xx*** in the 1.2−1.3 g cm^{-3} range and did not vary in any systematic fashion within each ALC.
(71) It is noted that this description is still just a first-order approximation: The issue of what combination of ALC, ALC concentration, and solvent is appropriate in order to minimize shrinkage and prevent collapse is convoluted further with the fact that longer ALC are expected to promote H-bonding between the −(OCH$_2$CH$_2$)− and the −NH(CO)− groups (see section 2.3.2), which reduces segmental motion of the polymeric chains.
(72) Tcharkhtchi, A.; Abdallah-Elhirtsi, S.; Ebrahimi, K.; Fitoussi, J.; Shirinbayan, M.; Farzaneh, S. Some New Concepts of Shape Memory Effect of polymers. *Polymers* **2014**, *6*, 1144−1163.
(73) Silverstein, R. M.; Bassler, G. C.; Morrill, T. C. *Spectroscopic Identification of Organic Compounds*, 5th ed.; John Wiley & Sons, Inc.: New York, 1991; pp 122−123.
(74) Silverstein, R. M.; Bassler, G. C.; Morrill, T. C. *Spectroscopic Identification of Organic Compounds*, 5th ed.; John Wiley & Sons, Inc.: New York, 1991; pp 112 and 120.
(75) McCarthy, S. J.; Meijs, G. F.; Mitchell, N.; Gunatillake, P. A.; Heath, G.; Brandwood, A.; Schindhelm, K. In-vivo Degradation of Polyurethanes: Transmission-FTIR Microscopic Characterization of Polyurethanes Sectioned by Cryomicrotomy. *Biomaterials* **1997**, *18*, 1387−1409.
(76) Sung, C. S.; Schneider, N. S. Temperature Dependence of Hydrogen Bonding in Toluene Diisocyanate Based Polyurethanes. *Macromolecules* **1977**, *10*, 452−458.
(77) Teo, L.-S.; Chen, C.-Y.; Kuo, J.-F. Fourier Transform Infrared Spectroscopy Study on Effects of Temperature on Hydrogen Bonding in Amine-Containing Polyurethanes and Poly(urethane-urea)s. *Macromolecules* **1997**, *30*, 1793−1799.
(78) Saito, Y.; Nansai, S.; Kinoshita, S. Structural Studies on Polyurethane Fibers. I. Crystal and Molecular Structures of Aliphatic Polyurethanes from Hexamethylene Diisocyanate and Some Linear Glycols. *Polym. J.* **1972**, *3*, 113−121.
(79) Christenson, C. P.; Harthcock, M. A.; Meadows, M. D.; Spell, H. L.; Howard, W. L.; Creswick, M. W.; Guerra, R. E.; Turner, R. B. Model MDI/butanediol Polyurethanes: Molecular Structure, Morphology, Physical and Mechanical Properties. *J. Polym. Sci., Part B: Polym. Phys.* **1986**, *24*, 1401−1439.
(80) Lee, H. S.; Wang, Y. K.; MacKnight, W. J.; Hsu, S. L. Spectroscopic Analysis of Phase-Separation Kinetics in Model Polyurethanes. *Macromolecules* **1988**, *21*, 270−273.
(81) It is noted that the extinction coefficient of free NH is about 3 times lower than that of H-bonded N−H.[75]
(82) Lendlein, A.; Kelch, S. Shape-Memory Polymers. *Angew. Chem., Int. Ed.* **2002**, *41*, 2034−2057.
(83) Liu, C.; Qin, H.; Mather, P. T. Review of Progress in Shape-Memory Polymers. *J. Mater. Chem.* **2007**, *17*, 1543−1558.
(84) Liu, C.; Chun, S. B.; Mather, P. T.; Zheng, L.; Haley, E. H.; Coughlin, E. B. Chemically Crosslinked Polycyclooctene: Synthesis, Characterization, and Shape Memory Behavior. *Macromolecules* **2002**, *35*, 9868−9874.
(85) http://www.reynoldsam.com/product/alja-safe/?gclid=CNaw_ciyw8kCFZI8gQod3JAGFQ.

DOI: 10.1021/acs.chemmater.7b01020
Chem. Mater. 2017, 29, 4461−4477

(86) http://www.aeromarineproducts.com/128-hgal-lp.html?gclid=CIHDjfm22ckCFQEcaQodUvsNyg.
(87) Standard Test Methods for Flexural Properties of Unreinforced and Reinforced Plastics and Electrical Insulating Materials: http://www.astm.org/DATABASE.CART/HISTORICAL/D790-10.htm.
(88) Standard Practice for Plastics: Dynamic Mechanical Properties: Determination and Report of Procedures: http://www.astm.org/Standards/D4065.htm).

DOI: 10.1021/acs.chemmater.7b01020
Chem. Mater. 2017, 29, 4461−4477